Response to reviews, ACP manuscript acp-2019-1173
Microphysics and dynamics of snowfall associated to a warm conveyor belt over Korea

Dear ACP Editor,
please find in this document our answers to the referees'comments. We hope that our corrections to the manuscript will make it suitable for publication in ACP.
Yours sincerely,
The authors of "Microphysics and dynamics of snowfall associated to a warm conveyor belt over Korea "

Reviewer #1

Review of Microphysics and dynamics of snowfall associated to a warmconveyor belt over Korea", by Josué Gehring, Annika Oertel, Étienne Vignon, Nicolas Jullien, Nikola Besic, and Alexis Berne, https://doi.org/10.5194/acp-2019-1173

Overview

This very interesting and well written article discusses their interpretation of the microphysics associated with snowfall associated with a warm conveyor belt that occurred over Korea on 28 February 2018. Their interpretations are based on air trajectories using the Integrated Forecast System Model, scanning X-band Doppler dual-polarization radar, vertically pointing W-band Doppler radar combined with an integrated 89 GHz radiometer, and the multi-angle snowflake camera located at the ground.

General Comments

The interpretations of the microphysics of ice particle growth in this storm system are based on air trajectories, scanning polarization radar data and vertically pointing cloud radar data, and the MASC instrument. At first, I thought that it would be difficult to interpret the microphysics (habits, etc), nucleation (secondary ice production) and growth processes within this storm system without the use of in-situ (aircraft or some type of balloon-borne device). I was unexpectedly surprised to find that indeed they were able to conduct this type of analysis and justify their analysis. I therefore strongly support the conclusions reached in their study.

We gratefully thank you for your review of our paper. We answer your line by line comments here below.

Specific Comments

Page 3, line 9: IFS model: A reference(s) is needed, and a brief description is desirable
Thank you for the suggestion, we added a reference on page 3, line 24:
"We also make use of the Integrated Forecast System (IFS, ECMWF (2017)) model from the European Center for Medium-Range WeatherForecast to identify WCB trajectories associated with this event."
and a reference of the model version and microphysics scheme used on page 5, line18:

"[..] on the 1-hourly 3D wind field of the hydrostatic model IFS (model version Cy43r3 operational from July 2017 to June 2018, ECMWF 2017), The details of the microphysics scheme can be found in Forbes et al. (2011)"

Page 6, line 20: 5 cm/s seems too low to maintain 100% RH in the presence of both ice and

snow.
Thank you for pointing this. We did the computation of the critical vertical velocity to maintain supercooled liquid water in the presence of both ice and snow this time, taking again the relation of Korolev and Mazin 2003 (Fig. 10). We found that a critical velocity of 10 cm/s would be enough to maintain liquid water with the concentrations and size distributions provided by the IFS data at 09 UTC in this event. Considering that the ascent rate of the WCB is 20 cm/s, we conclude that it is enough to maintain supercooled liquid water. We added the details of the calculation in an appendix of the paper, which can be found as a second answer to your post in the discussion. We modified this part in the manuscript consequently, Page 6, line 33:
"To show that the ascent rate of the WCB is large enough to produce SLW, we estimated wc from Fig. 10 in Korolev and Mazin (2003) using the radio-sounding and IFS data at 09:00 UTC at 4000 m asl. We found that in this event a vertical velocity greater than 0.1 m s^{-1} would form supercooled droplets in the presence of both ice and snow particles. The ascent rate of the WCB can be estimated from Fig. 4 to 0.2 m s^{-1}. We conclude that the simulated SLW is a consequence of the strong large-scale ascent in the WCB. "

Page 7, line 15: Figure 6 is terrific. It would be just great to use a V D =Z e relationship for snow to get a rough estimate of the air vertical velocity. If you want suggestions as to how to best do this, you can contact this reviewer (identified at the end of this review).
Thank you for this suggestion. According to our discussion, we decided to investigate the estimation of the air vertical velocity in future studies.

Page 7, 25: KH waves need a stable lapse rate. You mention later that the lapse rate supports KH waves, but you could mention it here. A suggestion would be to discuss the stability of the lapse rate from the sounding through the vertical column of the cloud.
Thank you for this suggestion. We looked at the vertical profiles of the gradient Richardson number (*Ri*) to investigate the conditions for KH instability. It is likely that between 3000 and 5000 m the observed updrafts can be generated by KH instability, since *Ri* is smaller than one and often smaller than 0.25. We added this sentence Page 8, line 6:
"Except for a moist neutral layer around 4000 m at 06:00 UTC, the profiles at 06:00 and 09:00 have a stable lapse rate, which together with a strong wind shear provide favourable conditions for Kelvin-Helmholtz instabilities."

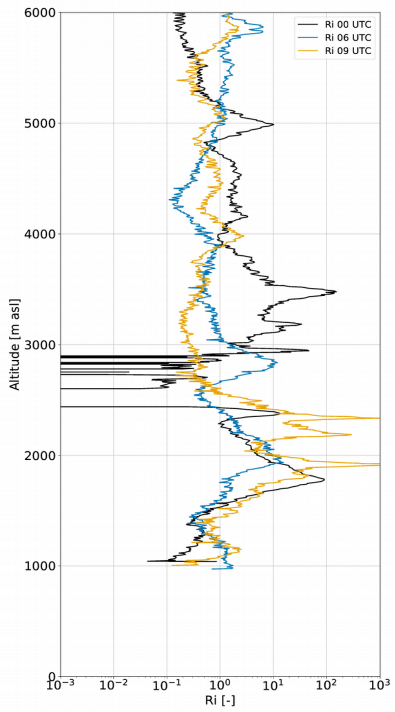

Figure 1: Gradient Richardson number computed from the radiosoundings

General Comment: I feel that you are placing too much accuracy on the measurements of the RH and thus RHi-see for example Page 9, lines 9-11.
We changed the indications of saturation to qualitative terms (e.g. well/slightly above saturation) instead of percentages.

Page 8, line 26, Fig 8: What was the collection temperature?
The average temperature of collection during the period 03:00 to 04:00 UTC was 1.5°C (see Fig. 6a). It is a good point, so we added the average temperature at the site during the collection periods in the MASC figures captions (Fig. 8, 11, 14) and we also mentioned it in the text when this information is relevant.

Technical Corrections

Page 4, line 2: national>National
Corrected
Page 6, line 7: probably should number this figure (6) as (5).
Page 6, line 29: Fig. 5>Fig. 6
We inverted the order of these figures.
Page 7, 11: Micvrophysial>Microphysical
This typo was corrected in the discussion paper published on 04 February 2020.
Page 8, line 31: "support" to "supports"
Corrected

Reviewer #2

General Comments:

The authors are to be commended for a manuscript and research that works toward answering a novel and important question in the study of precipitation processes. The leveraging of a suite of ground observations, combined with additional fields that must be obtained from NWP, works quite well to provide an analysis of this case. However, there are some important issues that need to be resolved before it should be accepted for publication. One of these issues, as I mention below, is fundamental to the entire purpose of this study, and therefore it is imperative that it be fully rectified.

We gratefully thank Reviewer #2 for his/her review our paper. We answer his/her line by line comments here below:

Specific Comments:

P2,L1-16: This section needs a brief discussion of Atmospheric Rivers (ARs) and IVT, and a few citations about them. The first question I would like answered in here is: "are WCBs and ARs the same thing by definition? Is every WCB, and every location within a WCB, an AR? Is every AR a WCB?" I have seen both in the literature but do not know the difference.
A good start for citations would be Rutz et al. (2014):
https://journals.ametsoc.org/doi/full/10.1175/MWR-D-13-00168.1
The reason I suggest it as a good start is the usage and definition of IVT. The current study uses IVT, but I cannot find it defined anywhere. Also, since Rutz et al. define an AR as having 250 kg m -1 s -1, the authors should consider beginning their IVT contours at 250 in Fig. 2.

Thank you for this suggestion. There exists some work in the literature that specifically addresses the difference between ARs and WCBs (Knippertz et al. 2018, Dacre et al. 2019). The main difference is that WCBs are Lagrangian features (e.g. relative to an extra-tropical cyclone) defined as trajectories with an ascent greater than 600 hPa in 48 hours (Madonna et al. 2014). Atmospheric rivers are Eulerian features defined as 2D objects poleward of 20° latitude with IWV>20 kg/m2, IVT>250 kg/m/s and longer than 2000 km. They can be collocated, but often occur in isolation. WCBs are directly linked to baroclinicity and have a maximum of occurrence in winter in the storm tracks. There exists a secondary maximum of occurrence in strong orographic lifting regions (e.g. Andes, Himalaya), but otherwise the ascent is provided by large-scale baroclinic forcing. ARs are more frequent in summer and can be linked to non-cyclonic systems (e.g. monsoons). There is also no ascent in the definition.

Since we do not use the concept of ARs in this study, we think it is better not to introduce it explicitly. If we do insert it, it will be either too short and might confuse the reader or too long and out of the scope of this study. Instead we provided one reference (Dacre et al., 2019) that addresses the difference between WCBs and ARs, so that a reader not familiar with the difference can easily access it. This reference is added on P2,L1-3:

"Quasi-Lagrangian analyses of mid-latitude baroclinic storms showed the existence of three distinctive airstreams (Carlson, 1980): the dry intrusion, the cold conveyor belt (Harrold, 1973; Browning, 1990; Schultz, 2001) and the warm conveyor belt (WCB, Green et al., 1966; Harrold, 1973; Browning et al., 1973; Dacre et al., 2019). "

Concerning the definition of IVT, we added the reference of Rutz et al. 2014, so that the reader not familiar with this variable can find the definition. We think it is out of the scope of this study to explicitly write the equation, since it is not a central variable of this study and it would be difficult to argue why we explicit this variable and not others (e.g. potential vorticity).

Regarding the start of the IVT contours: we tried with the first contour at 250 kg m^{-1} s^{-1}, but it decreases the overall readability of this figure (see Fig. 2 of this document) that already contains a lot of information. Since we focus on the most intense part of this atmospheric river, we decided to show only the values greater than 500 kg^{-1} m^{-1} s^{-1}. This information has been added in the caption of Fig. 2 of the paper, because it was missing.

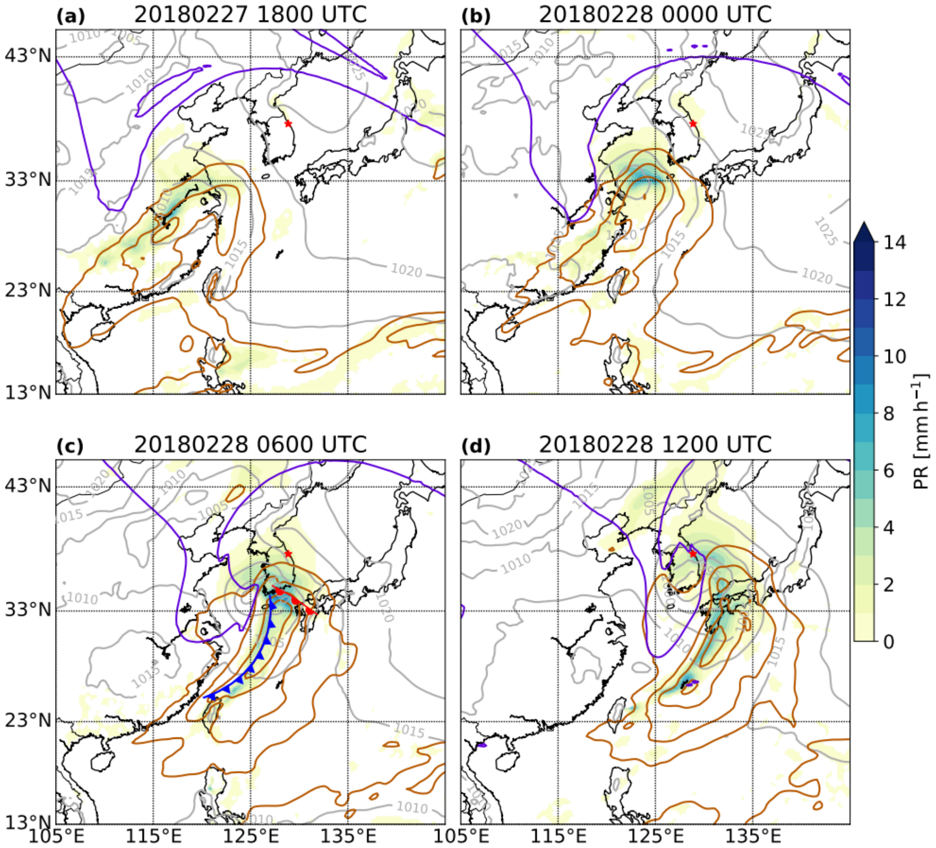

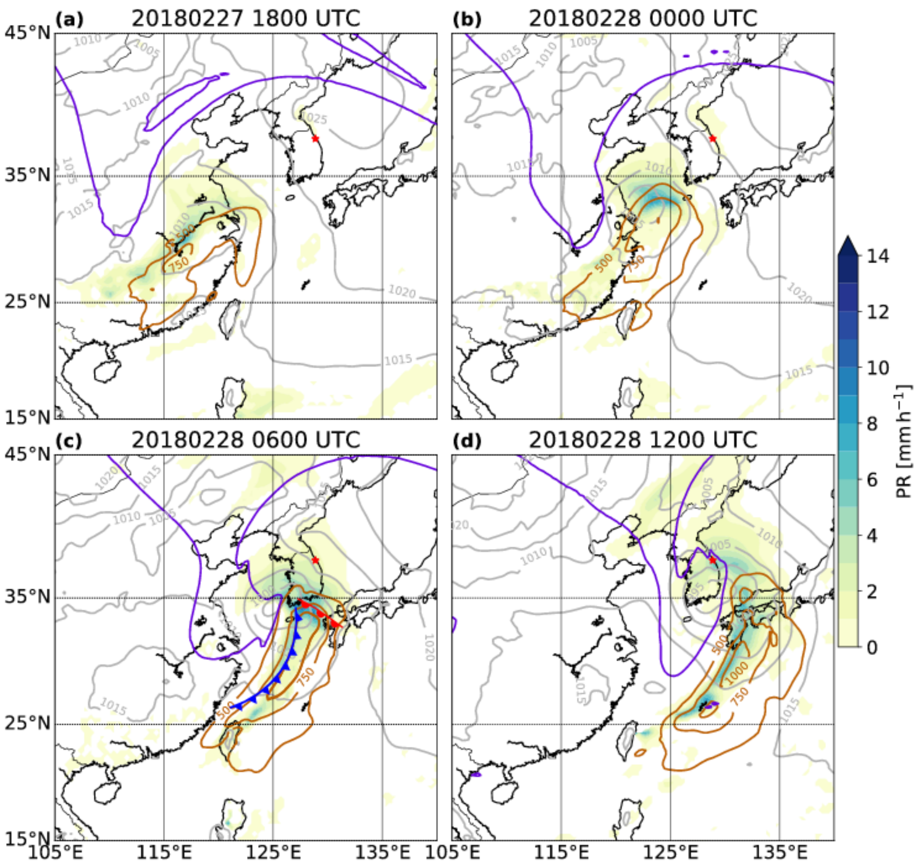

Figure 2: Same as Fig. 2 of the paper. (top) IVT starting at 250 kg^{-1} m^{-1} s^{-1}, (bottom) at 500 kg m^{-1} s^{-1}

P2,L22-30: This portion of the review needs improvement. The general suggestion is that the authors need to provide the reader with the relevant background on dual-pol signatures in ice-phase and mixed phase situations, so that they are prepared to properly interpret the upcoming results they are about to encounter.

We totally agree with this comment. We added the suggested information and other dual-polarisation signatures that are relevant for the interpretation of the results in this study. The modified introduction can be found in the latest version of the manuscript and in the track changes document.

Specific suggestions:

a) The sentence "Grazioli et al. (2015) suggested that similar peaks in Kdp can result from secondary ice generation" is not representative of the Grazioli work. This should be changed to "Grazioli et al. (2015) suggested that similar peaks in Kdp can result from secondary ice generation or the riming of ice crystals with anisotropic shapes."

Indeed, we changed it as suggested

b) There are three quotes in here (doi:10.15191/ nwajom.2013.0119) that contain great info for the reader:

"The exact value of ZDR depends on the crystal density; solid ice particles such as hexagonal plates can have intrinsic ZDR values larger than 6 dB, in some cases even approaching 10 dB (e.g., Hogan et al. 2002), whereas the ZDR in dendrites generally remains below about 4–5 dB. However, because of particle wobbling, imperfect shapes, and a mixture of crystal types usually present in clouds, observed ZDR values in ice crystals usually do not exceed about 4–5 dB."

"In contrast to the pristine ice crystals, large aggregates are observed to have very low ZDR (<0.5 dB). This is primarily attributable to their very low density (usually <0.2 g cm–3, compared to the density of solid ice of 0.92 g cm–3), which makes their exact shape less important from the radar's perspective. "

"Additionally, increased fluttering of aggregates tends to keep ZDR quite low. Note that, because of their large sizes compared to pristine crystals, snow aggregates tend to have larger ZH values. Observations of ZH increasing towards the ground coincident with ZDR decreasing towards the ground are consistent with ongoing aggregation." Please include this information (in a few sentences) in this section.

Thank you for these specific quotes. We included this information, together with an introduction of Kdp on P2,L25:

"For instance, differential reflectivity ZDR, defined as the logarithmic ratio between the reflectivity factor at horizontal and vertical polarisations (ZH−ZV in dB), is a measure of the reflectivity-weighted axis ratio of the targets (Kumjian, 2013). Oblate particles (e.g. raindrops, dendrites) have positive ZDR values, while prolate ones (e.g. vertically oriented ice in an electric field) exhibit negative ZDR values. ZDR also depends on the crystal density, but not on the number concentration. Therefore, large aggregates tend to have small ZDR (<0.5 dB, Kumjian 2013), primarily because they have a much lower density than solid ice, but also because they tend to be more spherical than pristine crystals. On the other hand, aggregates are much larger than crystals and tend to have higher ZH values. Consequently, decreasing ZDR together with increasing ZH towards the ground is a consistent sign of the aggregation process (Kumjian et al., 2014; Grazioli et al., 2015). Furthermore, the specific differential phase shift (Kdp in ◦ km^{-1}), which is the range derivative of the total differential phase shift on propagation (i.e. phase difference between the horizontal and vertical polarisation waves), is related to the axis-ratio, the density, the number concentration and the size of the targets. Being a lower order moment than ZH, it is more influenced by the number concentration, such that a high number concentration of small oblate crystals can lead to an increase of KDP, while ZDR will barely be affected. "

Figure 2: the authors should consider decreasing the size of the geographic domain of the subplots, as it would be easier to see what is happening over Korea. I know there is a need to see the broader environment for cyclogenesis, etc., but I think a sizable reduction could be accomplished without losing any important large-scale details. Also, the locations of the labels of IVT contours could be made smaller and moved to locations that have fewer things drawn over the top of one-another. For example, the 1000 label in 2c is probably not needed – the reader can infer that.

We slightly decreased the domain, mostly we reduced the eastern extent, but we kept the longitude minimum to 105° to see the PV streamer approaching. We decreased the size of the IVT contour labels and removed the 1000 kg^{-1} m^{-1} s^{-1} label on panel c (see Fig. 2 of this document). In this way, we think the plot is more readable.

P6,L10: why not also "(iii) advection of liquid droplets from below to above freezing level"? This would technically become new SLW, correct?
Or change the sentence to "The increase on LWC is likely a result of...", and the rest of the sentence would be correct.

Correct. We changed it to (P.6, L26): "The increase on LWC in supercooled conditions is likely a result of (i) condensation on the water droplets advected from below to above freezing level and (ii) nucleation of new droplets at subfreezing temperatures."

P8,L3: Does the partial melting of the hydrometeors at low levels during this warmest period help explain the spike in brightness temperature? Does the presence of liquid on the MASC hydrometeors correlate at all with this spike?

It is a very good point that we indeed did not address. Yes, before 07:00 UTC the temperature is above freezing at MHS and the peaks in brightness temperature correlates with the onset of precipitation at 04:00 UTC and the maximum of precipitation rate at 06:00 UTC. The former is due to a large proportion of wet particles (>50% Fig. 3 in this document), because the temperature is of 1°C (Fig. 6e of the paper). The latter is due to strong precipitation at temperatures slightly above freezing (0.2°C) leading to partly melting hydrometeors (~25%). So yes, for these two peaks there is a correlation with the presence of liquid water in the MASC images and it is consistent with the temperature above freezing. The peaks in brightness temperature after 07:00 UTC do not correlate with melting hydrometeors, but rather with updraughts. Since the temperature is below freezing after 07:00 UTC, it suggests the production of SLW. We modified this part in the manuscript as followed:
P8 L19:
"The maxima in brightness temperature observed when precipitation starts just before 04:00 UTC and at the peak at 06:00 UTC corresponding to the local maximum of precipitation rate (Fig. 5e), are probably due to partial melting of hydrometeors, since the near-surface temperature at MHS is above 0°C. The multiple peaks after 07:00 UTC (temperature below freezing), which are co-occurring with updraughts, suggest
that the updraughts favour the production of SLW in addition to the SLW produced by the large-scale ascent in the WCB."

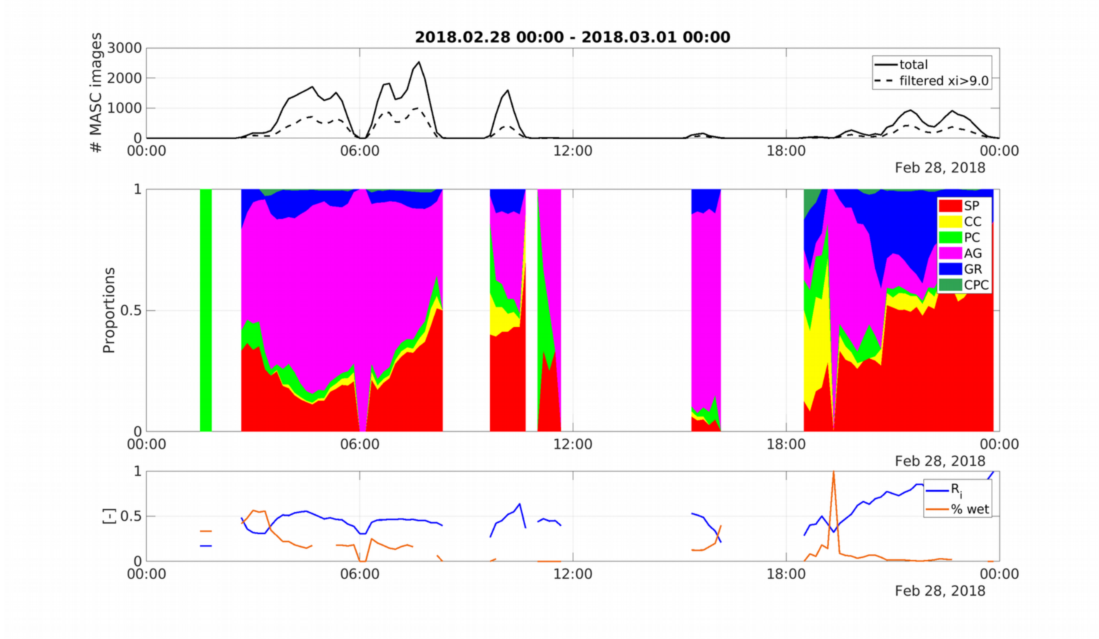

Figure 3: Time series of MASC data. (Top): number of images observed (dashed line those with a quality index greater than nine, see Praz et al. 2017). (Middle): hydrometeor classification. (Bottom): riming index (blue) and proportion of melting particles (orange).

Fig. 6d: please use a retrieval (perhaps from Küchler et al. 2017) to obtain LW content and add it to 6d. The brightness temperature by itself is helpful, but does quantify the LWC.

A reliable estimate of the LWC using the brightness temperature requires a large set of radiosondes data (Küchler et al. 2017), which we do not have for this location. The software of the WProf radar provides an estimation of the LWP based on ERA-I data, but the algorithm has not been trained for South-Korea. Rather than showing a LWP which we are not confident in, we decided to show the brightness temperature, which is the main variable determining the LWP. Since we only use this information qualitatively (i.e. its relative evolution with time), we think it is better to show the raw measurement of brightness temperature. We added the following information in the manuscript:
P.8 L.18: "The brightness temperature measured by the radiometer (Fig. 5d) is the primary variable used in estimations of the liquid water path (e.g. Küchler et al., 2017). In this study, we will use the brightness temperature as an indicator of the temporal evolution of the total liquid water in the atmospheric column."

P9,L1-3. As mentioned here, Fig. 8 indicates roughly the same fraction of graupel for this "vapour deposition" period as the fraction for Figs. 11 and 14. It also has the highest brightness temperature (and therefore LWC) of the entire study. It seems a bit odd to call this the "vapour deposition" period. I understand that the authors hypothesize that the riming happened below 2000 m, but that makes the claim of dominant vapor depositional growth during this period entirely dependent on the dual-pol hydrometeor classification scheme and inference from the sounding profile. It also undermines the main purpose of this study, as whatever mass was added by riming below 2000 m is quite important to the synoptic-microphysical connections that the authors are attempting to make in this paper. Where is this riming in the conceptual diagram (Fig. 16)? This is the most critical problem facing this manuscript.

Thank you for this comment, it is an important point in the manuscript that we had to address. The first point is that, even if the proportion of graupel is roughly the same for all periods, the number of particles and the precipitation intensity is much larger between 06-08 UTC. This means that the riming and aggregation processes taking place above 2000 m and which are directly linked to the

WCB, are the most relevant for the precipitation accumulation. This is the most important message of the manuscript.
The second point is that, because they are close to the resolution limit, small particles tend to appear more spherical and brighter, two important factors in the classification of MASC images in Praz et al. (2017). This artificially increases the riming index of small particles.

The third point is that the graupel category includes only fully rimed particles. The aggregates category contain all aggregates from dry to almost fully rimed. The riming index distribution of Fig. 1 clearly shows that if one removes graupel and small particles, the period from 06 to 08 UTC is the most rimed and this contribution comes from rimed aggregates. The main message of this period is that the WCB is responsible for significant riming and aggregation which leads to large-rimed aggregates and explain the large precipitation accumulation. The riming observed between 03-04 UTC is not contributing much to the overall precipitation accumulation.
We added the following on P.11 L.20:
“Note that while the previous period (Sec. 5.1) featured riming below 2000 m, the precipitation rate was much smaller than from 06:00 to 08:00 UTC (Fig. 5e) and hence this riming did not contribute significantly to the total precipitation accumulation. The important message here is that the flow conditions in the WCB promoted rapid precipitation growth by aggregation and riming above 2000 m and are thus responsible for the large precipitation accumulation between 06:00 to 08:00 UTC.“
The riming in the conceptual model is represented by the blue liquid droplets accreting to the snowflakes (below 500 hPa).

Section 5.1. Would extending this period to 0500 UTC allow for a selection of MASC images without liquid water on them? The surface temperature cools a bit from 0400 to 0500. This would also make it the same 2-hour length (and sample size of radar scans) as the other two periods.
Yes, but the period 04-05 UTC is already dominated by aggregation leading to large particles, while 03-04 UTC is dominated by small particles. If we combine the two periods, the size distribution is closer to the period 06-08 UTC (see Fig. 2). The idea behind the section “microphysical analysis of periods of interest” is to analyse time periods that contain consistent processes associated with different phases of the WCB (i.e. outflow, ascent), not necessarily of the same duration. If we extend the period to 05:00 UTC, then we have a mix of small particles which grow by vapour deposition in the outflow of the WCB air masses and others which aggregated in the turbulent layer appearing after 04:00 UTC. This would be less relevant for our analysis.

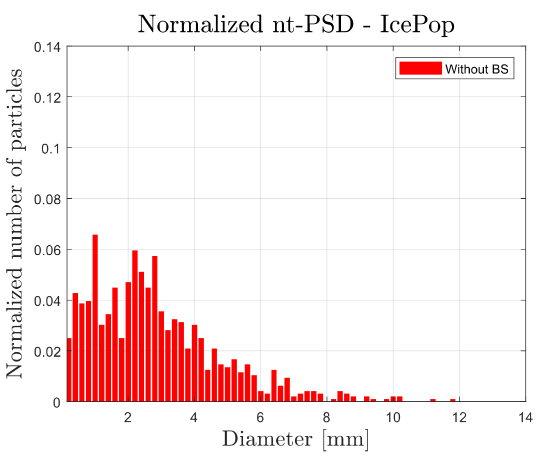

Figure 4: Normalised size distribution observed from 03:00 to 05:00 UTC.

P10,L5-7: It seems a bit optimistic to call any of those layers below 3000 m at 0600 potentially unstable. If those wiggles are averaged for even 200 m, there is a net increase in θ_e. "Moist neutral" is probably more accurate. The flow has strengthened from period 5.1, and in Fig. 6b, from 789–2000 m, I instead see increased turbulence from the stronger flow potentially playing a role. The intense vertical motion in the 3000–6000 m layer in Fig. 6b most definitely cannot be attributed to anything but turbulence from the intense shear. I would focus on the shear-induced turbulence as the mechanism for the lifting here, with perhaps a brief mention that there could be a small contribution of buoyancy from the wiggles in the θ_e" line.

Good point. The shear-induced turbulence might indeed be the main reason for the observed updraughts. Figure 3 shows the gradient Richardson number (*Ri*) from the three radio-soundings. Between 3000 and 6000 m, R_i is almost always below 1 for all three radio-soundings and sometimes below 0.25, which suggests indeed that the turbulence is shear-generated.

We removed the sentence P.10,L5:

"Moreover the layers of potential instability below 3000 m (Fig. 5a) indicate that instability can be released, if sufficient lifting is provided, for instance by the Kelvin-Helmholtz waves."

and modified P11,L1:

"These sources of lifting together with the moist neutral layers below 3000 m (Fig. 6a) can lead to the observed strong updraughts (Fig. 5b), which promote aggregation by increasing the probability of collisions between particles."

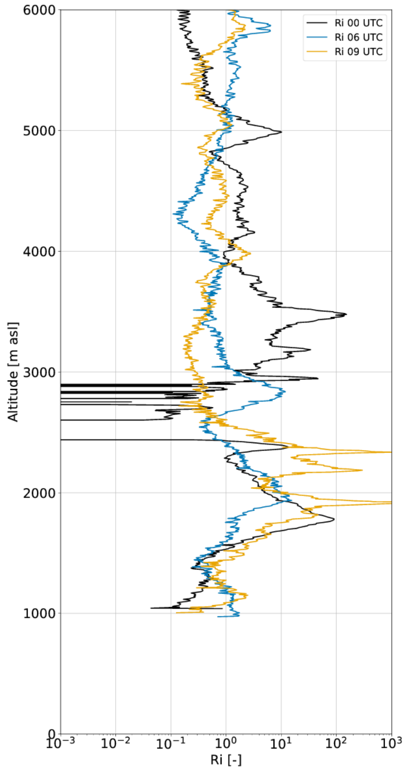

Figure 5: Gradient Richardson number computed from the radiosoundings

P10,L24-P11,L4: This section does not add much to the paper. The updraught being discussed is already the most salient feature in Fig. 6b, and Figs. 12 and 13 do not provide much in the way of information that cannot be gleaned from Figs. 6a,b. I would suggest dramatically shortening this section.

We decided to remove Fig. 13 and its corresponding discussion (P. 11, L 5-9), because indeed it does not add much to the paper. However we decided to keep Fig. 12 and its interpretation, because we think that the discussion on the increase of the spectral width during the updraught is relevant to show that the updraughts are responsible for the increases in turbulence and hence aggregation. The fact that in Fig. 12b the spectral reflectivity increases with a decrease in Doppler velocity further supports this hypothesis of strong aggregation in the turbulent layer and fall of the hydrometeors once they grew big enough to compensate for the updraught. The subsequent discussion on the timing of the strong updraught and the increase in precipitation intensity is relevant for our hypothesis that the embedded convection is responsible for the strongest precipitation observed.

P11,L2-4: Why does this suggest that convection is responsible? There is no substantial evidence to support that conclusion. There is no instability anywhere near this level in the 0600 sounding, and why could it not be a particularly strong KH billow?

The cause of this updraught cell with a vertical extent of 2000 m cannot be directly assessed with the radio-soundings at 06:00 and 08:00 UTC. However it is very consistent with embedded convection within warm frontal cloud as observed by Hogan et al. 2002, Keppas et al. 2018 and Oertel et al. 2019. Hogan et al. 2002 showed that Kelvin-Helmholtz instability can generate embedded convection. In addition the radio-sounding at 06:00 UTC shows a strong shear just below

4000 m exactly where the strong updraught cell starts. This probably generated the updraught cell, which continue to propagate upwards. Just below 6000 m, where the updraught cell stops, there is a stable layer of about 100 m, which might have stopped the updraughts.
We did not find any case in the literature of such vertically extended KH billows. In addition the term embedded convection is often used without a specific mention of static instability (Hogan et al. 2002, Keppas et al. 2018). However, since we cannot evidence the presence of convective instability, we decided to replace the occurrences of "embedded convection" that were referring specifically to this case with embedded updraught. We added a sentence in this direction on P.8, L14:
"While the cause of the updraughts we observe might be different than those mentioned in Hogan et al. (2002), Keppas et al. (2018), Oertel et al. (2019a), the consequence on precipitation growth processes is consistent with what we observe in this study."

P11,L3: It would be more convincing if the "intense riming" were obvious in the MASC image (Fig. 11). If anything, the riming in period 5.3 (Fig. 14) seems more intense to my eye, but it is difficult to assess with much certainty from the images. Was there any sort of disdrometer, especially a PARSIVEL, available at the site? If so, the density of the hydrometeors could be calculated from it. If the density were compared for particles of similar size, this would provide a more precise quantification of the degree of riming than the MASC.
According to Battaglia et al. 2010, fall velocity measurements of solid hydrometeors from PARSIVEL lead to an underestimation of up to 20%. Instead, the MASC can provide the riming index together with fall velocity measurements, which we are more confident on the accuracy, since it was installed in a DFIR. From Fig. 6, it is clear that the period 06-08 UTC has larger riming index and, despite lower quartiles, has larger maximum fall-speeds than the period 03-04 UTC.

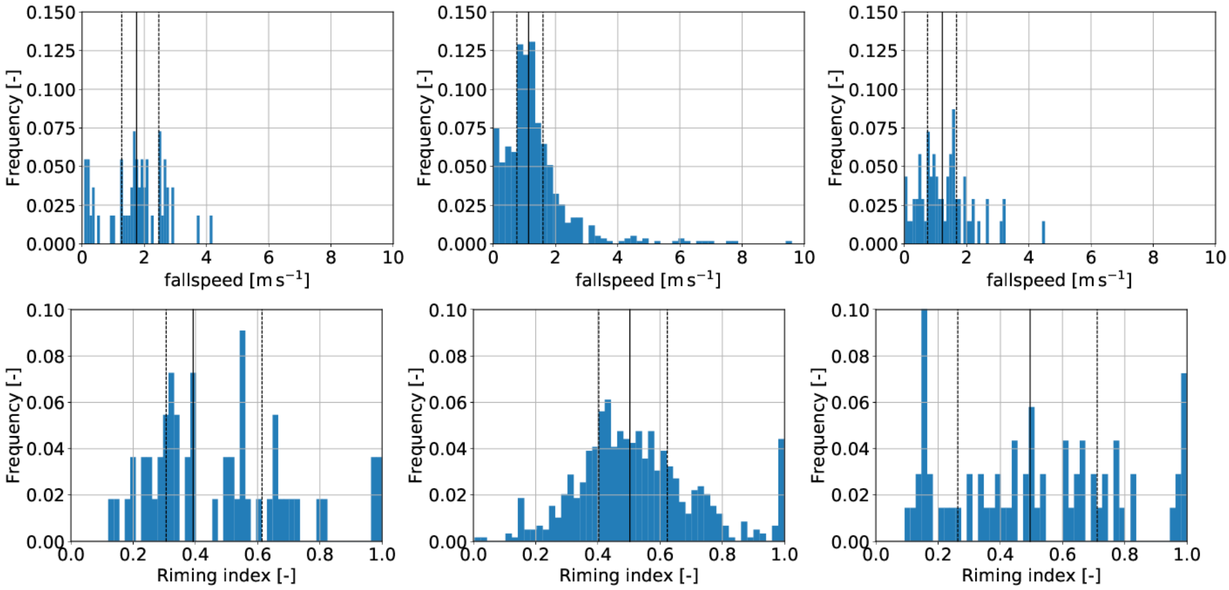

Figure 6: (Top) Distribution of fallspeeds for (left) 03-04 UTC, (middle) 06-08 UTC, (right) 09-11 UTC. (Bottom): same for riming index.The dashed lines shows the 25th and 75th percentiles of the distribution, the solid line shows the median.

P11,L13: "there are substantially more crystals and graupel particles than during other periods". This is true of the crystals, but the graupel concentrations are 9.1%, 8%, and 9.2% for the respective periods. I'd say that's about the same amount of graupel for each period.
True, we removed "and graupel particles" from this sentence. This is related to the limitations of the classification of small particles in MASC images (see above).

P12,L11-12: The authors attribute the change from low Kdp in period 5.1 to high Kdp in 5.2 and 5.3 to the appearance of secondary ice. However, it seems there are two other possibilities. (1) as the authors mention, the number concentration of crystals is low in 5.1, and the greater concentrations of oblate targets/more intense precipitation in 5.2 and 5.3 are responsible for the increased Kdp. (2) The crystals in 5.1 are lightly rimed, and the onset of heavier riming in 5.2 and 5.3 is responsible for the increased Kdp. Please discuss this somewhere, and explain why either or both of those hypotheses can be ruled out.

Thank you for this comment. We did not properly address the effect of precipitation intensity and increase in concentration in the Kdp signature. We hypothesise that the increase in Kdp compared to period 5.1 is primarily due to the increase in precipitation intensity, but that the fact that it is collocated with aggregation and riming needs another mechanism to produce a high number concentration of oblate particles. We added this explanation on P10,L22:

"Note that the higher Kdp values compared to the period 03:00-04:00 UTC is primarily due to the increase in precipitation intensity, but the fact that Kdp increases below the onset of aggregation cannot be explained by precipitation intensity only, since aggregation decreases the number concentration and the oblateness of the particles. Riming initially increases Kdp by first filling cavities and hence increasing the density of particles, but later on leads to a decrease in Kdp as the rime mass will smooth the particles' shape. There has to be a mechanism which produces a high number concentration of oblate particles to explain an increase in Kdp in a layer dominated by aggregation and riming."

Technical Corrections:

Multiple Locations: the phrase "associated to" would be more correctly written as "associated with".

Thank you, we corrected it.

Multiple Locations: is there a "Wernli" and a "Werni" citation, or is this a typo? Correct throughout the manuscript.

We corrected this typo.

P5,L27: change "more and more" to "increasingly"

We corrected it.

Fig 5. Can the authors plot wind barbs somewhere on here? It helps to visualize the shear layers.

We think it would decrease the visibility of the figure to add three (one per sounding) wind profiles with wind barbs. We could replace the wind speed and direction plots by wind barbs only, but we prefer to keep them, as it allows a direct reading of speed and direction values.

Fig. 6. Please enlarge the figure slightly if possible. The details in 6c are the most difficult to see.

We increased the width of this figure.

Fig. 6c: please add a colorbar with labels for the hydrometeor information, instead of listing it in the caption – I don't know what "cerise" is, and there appear to be more colors than you describe in the caption. Please also provide a citation for the hydrometeor classification algorithm that is used.

We added the legend and changed the colours: now rimed particles are in red, which is easier to see. We also added the reference of the classification algorithm in the caption. The updated figure and its caption can be found at the end of this document.

Figs. 7, 9, 15: Please add a 5th subplot of temperature. Shouldn't the line corresponding to the lower limit of the WCB change for each period?
We added the temperature subplot. We also corrected the line corresponding to the lower limit of the WCB. The updated figures and their captions can be found at the end of this document.

Fig. 15. Caption should instead say "Same as Fig. 7", correct?
Correct, thank you for pointing that. We corrected it.

References

Dacre, H. F., Martínez-Alvarado, O., and Mbengue, C. O.: Linking Atmospheric Rivers and Warm Conveyor Belt Airflows, Journal of Hydrometeorology, 20, 1183–1196, https://doi.org/10.1175/jhm-d-18-0175.1, 2019.

Hogan, R. J., Field, P. R., Illingworth, a. J., Cotton, R. J., and Choularton, T. W.: Properties of embedded convection in warm- frontal mixed-phase cloud from aircraft and polarimetric radar, Quarterly Journal of the Royal Meteorological Society, 128, 451–476, https://doi.org/10.1256/003590002321042054, http://dx.doi.org/10.1256/003590002321042054, 2002.

Keppas, S. C., Crosier, J., Choularton, T. W., and Bower, K. N.: Microphysical properties and radar polarimetric features within a warm front, Monthly Weather Review, 146, 2003–2022, https://doi.org/10.1175/MWR-D-18-0056.1, 2018. Knippertz, P., Wernli, H., Binder, H., Böttcher, M., Joos, H., Madonna, E., Pante, G.,

and Sprenger, M.:The Relationship between Warm Conveyor Belts, Tropical Moisture Exports and Atmospheric Rivers, 20th EGU General Assembly, EGU2018, Proceedings from the conference held 4-13 April, 2018 in Vienna, Austria, p.4362, 20, 4362, URL https://presentations.copernicus.org/EGU2018-4362 presentation.pdf, 2018.

Madonna, E., Wernli, H., Joos, H., and Martius, O.: Warm conveyor belts in the ERA-Interim Dataset (1979-2010). Part I: Climatology and potential vorticity evolution, Journal of Climate, 27, 3–26, https://doi.org/10.1175/JCLI-D-12-00720.1, 2014.

Microphysics and dynamics of snowfall associated ~~to~~ with a warm conveyor belt over Korea

Josué Gehring[1], Annika Oertel[2], Étienne Vignon[1], Nicolas Jullien[3], Nikola Besic[4], and Alexis Berne[1]

[1]Environmental Remote Sensing Laboratory, École Polytechnique Fédérale de Lausanne (EPFL), Lausanne, Switzerland
[2]Institute for Atmospheric and Climate Science (IAC), Eidgenössische Technische Hochschule Zürich (ETH), Zurich, Switzerland
[3]Department of Geosciences, University of Fribourg, Fribourg, Switzerland
[4]Centre Météorologie Radar, Météo France, Toulouse, France

Correspondence: Alexis Berne (alexis.berne@epfl.ch)

Abstract. On 28 February 2018, 57 mm of precipitation associated ~~to~~ with a warm conveyor belt (WCB) fell within 21 h over South Korea. To investigate how the large-scale circulation influenced the microphysics of this intense precipitation event, we used radar measurements, snowflake photographs and radiosounding data from the International Collaborative Experiments for Pyeongchang 2018 Olympic and Paralympic winter games (ICE-POP 2018). The WCB was identified with trajectories computed with analysis wind fields from the Integrated Forecast System global atmospheric model. The WCB was collocated with a zone of enhanced wind speed of up to 45 $\mathrm{m\,s^{-1}}$ at 6500 m a.s.l., as measured by a radiosonde and a Doppler radar. Supercooled liquid water (SLW) with concentrations exceeding 0.2 $\mathrm{g\,kg^{-1}}$ was produced during the rapid ascent within the WCB. Vertical profiles of polarimetric radar variables show during the most intense precipitation period a peak and subsequent decrease in differential reflectivity as aggregation starts. Below the peak in differential reflectivity, the specific differential phase shift continues to increase, indicating early riming of oblate crystals and secondary ice generation. We hypothesise that the SLW produced in the WCB led to intense riming. Moreover, embedded ~~convection~~ updraughts in the WCB and turbulence at its lower boundary enhanced aggregation by increasing the probability of collisions between particles. This suggests that both aggregation and riming occurred prominently in this WCB. This case study shows how the large-scale atmospheric flow of a WCB provides ideal conditions for rapid precipitation growth involving SLW production, riming and aggregation. Future microphysical studies should also investigate the synoptic conditions to understand how observed processes in clouds are related to the large-scale circulation.

1 Introduction

Precipitation is the result of a chain of meteorological processes ranging from the synoptic to the micro scales. In particular for stratiform precipitation, the large-scale flow drives the transport of moisture and lifting of air masses, while microphysics ultimately determine the growth and fall of hydrometeors, influencing precipitation intensity and accumulation. Therefore understanding the link between large-scale flow and microphysics is paramount to better forecast precipitation. Extratropical cyclones are the main synoptic-scale features associated with precipitation in the mid-latitudes and produce more than 80 % of the total precipitation in the Northern Hemisphere storm tracks (Hawcroft et al., 2012).

Quasi-Lagrangian analyses of mid-latitude baroclinic storms showed the existence of three distinctive airstreams (Carlson, 1980): the dry intrusion, the cold conveyor belt (Harrold, 1973; Browning, 1990; Schultz, 2001) and the warm conveyor belt (WCB, ~~Green et al., 1966; Harrold, 1973; Browning et al., 1973~~Green et al., 1966; Harrold, 1973; Browning et al., 1973; Dacre et al., 201). The latter can be defined as a coherent warm and moist airstream rising from the boundary layer to the upper troposphere in about two days (Eckhardt et al., 2004; Madonna et al., 2014). Climatological studies of WCBs have used a simple criterion on the ascent rate of trajectories (e.g. 600 hPa in 48 h, Madonna et al. 2014).

WCBs typically rise from below 900 hPa to about 300 hPa and temperature along this flow typically decreases from above 0 °C to below -40 °C. Therefore, clouds along WCBs feature the whole spectrum from warm clouds to mixed-phase to pure ice clouds (e.g. Joos and Wernli, 2012; Madonna et al., 2014). WCBs are the primary precipitation producing feature in extratropical cyclones (Browning, 1990; Eckhardt et al., 2004) and are responsible for more than 70 % of precipitation extremes in the major storm tracks (Pfahl et al., 2014). However, precipitation and cloud processes also impact the dynamics of extratropical cyclones. Trajectory analyses showed that WCBs experience a strong cross-isentropic ascent due to latent heat release (Madonna et al., 2014), which leads to an increase in potential vorticity (PV) below the maximum diabatic heating level and a decrease above it (Wernli and Davies, 1997). This represents a direct link between microphysics and dynamics. Joos and Wernli (2012) studied the impact of different microphysical processes on the diabatic PV production in WCBs. They suggested that condensation of cloud liquid and depositional growth of snow and ice are the most important diabatic heating processes in WCBs. Joos and Forbes (2016) showed the direct impact of specific microphysical processes on the PV modification in WCBs and the subsequent downstream flow evolution.

Colle et al. (2014) studied the distribution of snow crystal habits within mid-latitude baroclinic storms over Long Island, New York. They observed moderately rimed crystals in the middle of the comma head, while heavy riming was present close to the cyclone centre. They also showed a positive correlation between vertical wind speeds, turbulence and degree of riming by means of Doppler data from a micro rain radar. Overall, this study highlights the spatial structure of microphysics occurring in winter storms and suggests a link between the dynamics of the cyclone and observed snow crystal habits.

Dual-polarisation Doppler (polarimetric) radars are useful to study precipitation microphysics~~and dynamics. First, ,~~ as they provide information on the hydrometeors' shape, density and phase. ~~Secondly, they allow indirect measurements of wind and turbulence. They~~ For instance, differential reflectivity Z_{DR}, defined as the logarithmic ratio between the reflectivity factor at horizontal and vertical polarisations ($Z_H - Z_V$ in dB), is a measure of the reflectivity-weighted axis ratio of the targets (Kumjian, 2013; Bringi and Chandrasekar, 2001). Oblate particles (e.g. raindrops, dendrites) have positive Z_{DR} values, while prolate ones (e.g. vertically oriented ice in an electric field) exhibit negative Z_{DR} values. Z_{DR} also depends on the crystal's dielectric constant, but not on the number concentration. Therefore, large aggregates tend to have small Z_{DR} (<0.5 dB, Kumjian 2013), primarily because they have a much lower density than solid ice, but also because they tend to be more spherical than pristine crystals. On the other hand, aggregates are much larger than crystals and tend to have higher Z_H values. Consequently, decreasing Z_{DR} together with increasing Z_H towards the ground is a consistent signature of the aggregation process (Schneebeli et al., 2013; Kumjian et al., 2014; Grazioli et al., 2015). Furthermore, the specific differential phase shift (K_{dp} in $^\circ\,\mathrm{km}^{-1}$), which is the range derivative of the total differential phase shift on propagation (i.e. phase difference between the horizontal and vertical polarisation waves propagating forward), is related to the axis-ratio, the density, the number concentration and the size of the targets. Being a lower order moment than Z_H, it is more influenced by the number concentration, such that a high number concentration of small oblate crystals can lead to an increase of K_{dp}, while Z_{DR} will barely be affected. Owing to this wealth of information, polarimetric variables have been extensively used for snowfall microphysical studies (Bader et al., 1987; Andrić et al., 2013; Schneebeli et al., 2013; Moisseev et al., 2015; Grazioli et al., 2015). The pioneering work of Bader et al. (1987) showed that high ~~differential reflectivity (~~Z_{DR} ~~)~~ values are associated ~~to~~ with large dendritic crystals. More recently, Moisseev et al. (2015) found that enhanced values of specific differential phase (K_{dp}) are related to the onset of aggregation, producing early aggregates that can be oblate. Grazioli et al. (2015) suggested that similar peaks in K_{dp} can result from secondary ice generation (leading to a high number concentration of small anisotropic crystals) or the riming of oblate ice crystals, which increases their density. These studies thoroughly analysed dual-polarisation signatures of snowfall microphysics. However, they did not consider the interactions between large-scale flow and microphysics. Keppas et al. (2018) studied the microphysical properties of a warm front with radar and in situ measurements in clouds. They found that a WCB formed a widespread mixed-phase cloud by producing significant amount of liquid water, which favoured riming and secondary ice generation. However, they did not formally identify WCB trajectories nor did they confirm that the liquid water was produced within the WCB. There is hence a need to better understand how the strong, coherent ascending motion within WCBs influences precipitation microphysics. To this end, a synergy between remote sensing and in situ measurements as well as trajectory analyses is needed.

In this study, we use data from the International Collaborative Experiments for Pyeongchang 2018 Olympic and Paralympic winter games (ICE-POP 2018) campaign to study an extreme snowfall event associated ~~to~~ with a WCB over South Korea on 28 February 2018. The location of Pyeongchang on a peninsula at mid-latitudes offers an interesting setting to study the interplay between the synoptic circulation, orographic effects and microphysics. First, the surrounding Yellow Sea and East Sea provide nearby sources of moisture for precipitation, which is particularly relevant for wintertime WCBs (Pfahl et al., 2014). Secondly, WCBs play a crucial role for precipitation over the Korean peninsula: between 80 $\%$ and 90 $\%$ of extreme precipitation is associated with WCBs in South Korea according to a climatological study by Pfahl et al. (2014). The ICE-POP 2018 dataset includes, among others, multiple frequency radar measurements and high-resolution snowflake photographs. We also make use of the Integrated Forecast System (IFS, ECMWF (2017)) model from the European Center for Medium-Range Weather Forecast to identify WCB trajectories associated ~~to~~ with this event.

To understand the role of the WCB during this intense precipitation event in Korea, we will address the following questions:

- What was the synoptic situation leading to this intense snowfall event?
- Which microphysical processes were involved?
- How did the specific flow conditions in the WCB influence the observed microphysics?

The paper is structured as follows. We will first introduce the measurement campaign and data sets in Sect. 2. The synoptic situation is presented in Sect. 3. Section 4 shows the evolution of the event over Pyeongchang. An analysis of the microphysics observed by radar and snowflake images during succeeding periods of interests is presented in Sect. 5. We then summarise the key findings of this study with a conceptual model in Sect. 6 before concluding in Sect. 7.

2 Measurement campaign and data set

ICE-POP 2018 was a measurement campaign organised by the Korea Meteorological Administration and supported by the World Meteorological Organisation. Figure 1 shows the location of Pyeongchang and the measurement sites. One of the main goals of ICE-POP 2018 is to improve our understanding of orographic precipitation in the Taebaek mountains (the mountain range along the east coast of the Korean peninsula in Fig. 1). To this purpose remote sensing and in situ measurements of cloud and precipitation were conducted in the Pyeongchang and Gangneung provinces between November 2017 and May 2018. In this study, we will focus on the data collected by an X-band Doppler dual-polarisation radar (hereafter MXPol), a W-band Doppler cloud profiler (hereafter WProf) and a multi-angle snowflake camera (hereafter MASC), details of which are provided in the following subsections. In addition, we will use measurements from a Pluvio^2 weighing rain gauge located in the Mayhills site (MHS, Fig. 1). Finally, we will show radiosondes (3-hourly resolution) and temperature measurements from Daegwallyeong (DGW) located 2 km away from MHS.

2.1 X-band Doppler dual-polarisation radar

MXPol was installed on top of a building in the Gangneung Wonju ~~national~~ National University (GWU) at the coast of the East Sea (Fig. 1). MXPol operates at 9.41 GHz with a typical angular resolution of 1°, range resolution of 75 m, non-ambiguous range of 28 km and a Nyquist velocity of 39 $\mathrm{m\,s^{-1}}$ in dual-pulse pair (DPP) mode or 11 $\mathrm{m\,s^{-1}}$ in fast-Fourier transform (FFT) mode (see Schneebeli et al., 2013 for more details). The scan cycle was composed of three hemispherical range height indicators (RHIs) at 225.8°(in FFT), 233°(in DPP) and 325.7°(in DPP) azimuth. The first two are towards MHS, while the third is perpendicular to this direction following the coast (red dashed lines in Fig. 1). The RHIs were performed with a range resolution of 75 m and an extent of 27.2 km. The cycle was completed by one plan position indicator (PPI) in DPP mode at 6°elevation (red dashed circle in Fig. 1) and one PPI in FFT mode at 90°elevation (for Z_{DR} monitoring). The PPI at 6°elevation had a range resolution of 75 m and an extent of 28.4 km. The scan cycle had a 5 min duration and was repeated indefinitely. The main variables retrieved from MXPol measurements are the reflectivity factor at horizontal polarisation Z_H (dBZ), Z_{DR} (dB), K_{dp} ($^\circ\,\mathrm{km^{-1}}$), the mean Doppler velocity ($\mathrm{m\,s^{-1}}$) and the Doppler spectral width SW ($\mathrm{m\,s^{-1}}$). During the FFT scans the full Doppler spectrum at 0.17 $\mathrm{m\,s^{-1}}$ resolution was retrieved. A semi-supervised hydrometeor classification (Besic et al., 2016) was applied on the polarimetric variables. A recently developed demixing module of this method (Besic et al., 2018) was also used to estimate the proportions of hydrometeor classes within one radar volume, which allows to study mixtures of hydrometeors.

2.2 W-band Doppler cloud profiler

WProf was deployed in MHS, 19 km inland of GWU at 789 m a.s.l. WProf is a frequency modulated continuous wave (FMCW) radar operating at 94 GHz, sampling the vertical column above the radar using typically three vertical chirps (Table 1). It consists of one transmitting and one receiving antenna. A comparison of MXPol and WProf specifications can be found in Table 2. WProf has an integrated passive radiometer at 89 GHz, which provides the brightness temperature of the vertical column above the radar (see Küchler et al., 2017 for more details).

2.3 Multi-angle snowflake camera

The MASC was deployed in a double fence wind shield in MHS. It is composed of three coplanar cameras separated by an angle of 36°. As hydrometeors fall in the triggering area, high resolution stereographic pictures are taken and their fall speed is measured. A complete description of the MASC can be found in Garrett et al. (2012). The MASC images were used as input parameters to a solid hydrometeor classification algorithm. Each individual particle is classified into six solid hydrometeor types, namely small particles (SP), columnar crystal (CC), planar crystal (PC), combination of column and plate crystal (CPC), aggregate (AG) and graupel (GR). In addition, the maximum dimension (diameter of the circumscribed circle) of particles is measured to characterise the size of the snowflakes. A detailed explanation of the algorithm is provided in Praz et al. (2017). One challenge during measurements of snowflakes in free-fall is the contamination from blowing snow. Schaer et al. (2018) developed a method to automatically identify blowing snow particles in MASC images. Despite the presence of a double fence wind shield during ICE-POP 2018, 31 % of the particles were identified as blowing snow and removed for this study. We will make use of particle size distributions estimated from the maximum diameter of particles following the work of Jullien et al. (2019).

2.4 Warm conveyor belt trajectory computation

We define the large-scale WCB ascent over the Korean peninsula in a Lagrangian perspective as a coherent ensemble of trajectories with an ascent rate of at least 600 hPa in 48 h (Wernli and Davies, 1997; Madonna et al., 2014). The 48-h trajectories were computed with the Lagrangian analysis tool LAGRANTO (Wernli and Davies, 1997; Sprenger and Wernli, 2015) based on the 1-hourly 3D wind field of the ~~IFS. The IFS~~ hydrostatic model IFS (model version Cy43r3 operational from July 2017 to June 2018, ECMWF 2017). The details of the microphysics scheme can be found in Forbes et al. (2011). The IFS is run with a spatial resolution of O1280 (approximately 9 km) and 137 vertical hybrid pressure-sigma levels (ECMWF, 2017). The IFS dataset combines operational analyses at 00:00, 06:00, 12:00 and 18:00 UTC with hourly short-term forecasts in between. The dataset was interpolated to a latitude/longitude grid with 0.5° spatial resolution for trajectory computation. To analyse the air parcel ascent in the vicinity of the measurement site, we combine 24-h backward and 24-h forward trajectories starting every hour between 00:00 UTC 27 February and 00:00 UTC 01 March 2018 every 50 hPa from 1000 hPa to 200 hPa in proximity of Pyeongchang. WCB trajectories are subsequently selected as trajectories exceeding an ascent rate of 600 hPa in 48 h. In addition to this Lagrangian representation (i.e. following the trajectories), we projected the WCB trajectories in an Eulerian reference frame above PyeongChang. This gives, for each time steps and for all vertical levels, the position of trajectories above PyeongChang which ascended with ascent rates of at least 600 hPa in 48 h within the period 00:00 UTC 27 February and 00:00 UTC 01 March 2018. This highlights at which heights WCB air parcels (i.e. with strong ascent at any given time) occur.

3 Synoptic overview and WCB

The 28 February 2018 precipitation event is the most intense of the whole ICE-POP 2018 campaign. It contributed 77 $\%$ of the winter 2018 (December–February) precipitation accumulation. At 18:00 UTC 27 February 2018 (Fig. 2a) a PV streamer (equatorwards excursion of stratospheric air) was located over eastern China and moved eastward towards South Korea. At 00:00 UTC 28 February 2018, (Fig. 2b) a surface cyclone has formed in the Yellow Sea east of the upper-level PV streamer. Towards 06:00 UTC, the surface cyclone intensified as the PV streamer was approaching (Fig. 2c) and became fully developed with a cold front passing to the south of the Korean peninsula and a warm front passing over Pyeongchang. The interaction between the upper-level PV streamer and the surface cyclone led to a rapid deepening of the cyclone by 25 hPa between 18:00 UTC 27 February and 12:00 UTC 28 February. The integrated vapour transport (IVT, Rutz et al., 2014) contours show the strong moisture flux ahead of the cold front with the most intense precipitation close to the cyclone center, where the IVT gradient is the largest. At 12:00 UTC the cyclone moved further east and the PV streamer was located over Korea inducing ~~a more and more~~ an increasingly easterly flow (Fig. 2d). While the Yellow Sea is a known region of cyclogenesis, the cyclone frequency over Korea in winter is less than 2 $\%$ (Wernli and Schwierz, 2006), indicating that such a synoptic situation in winter over Korea is relatively rare.

This intense precipitation event is associated with a WCB that ascends from the boundary layer to the upper troposphere and rises over the Korean peninsula during 28 February when the low pressure system was fully developed. Figure 3 shows an ensemble of trajectories that are part of the large-scale WCB airstream and that ascended near Pyeongchang at 06:00 UTC 28 February 2018. The inflow part of the WCB (i.e. upstream of the strong ascent in Fig. 3a) is characterised by IVT values greater than 1000 $\mathrm{kg\,m^{-1}\,s^{-1}}$, showing that the WCB transports large amounts of water vapour originating from the Yellow Sea. The trajectories are rapidly ascending over South Korea and liquid water content (LWC) increases along the selected WCB trajectories to above 0.2 $\mathrm{g\,kg^{-1}}$ in the region of strong ascent (Fig. 3b). The WCB ascent in the vicinity of the measurement site is relatively fast with ascent rates of approximately 500 hPa in 12 h (Fig. 4). During the relatively strong ascent from the boundary layer to the upper troposphere an extended mostly stratiform cloud band formed, which was also responsible for the surface precipitation (Fig. 5a,e). The WCB transported and formed up to 0.20 $\mathrm{g\,kg^{-1}}$ of liquid water during its strong ascent in the mid-troposphere (Figs. 3b and 4). The 0 $^{\circ}\mathrm{C}$ isotherm was higher than 900 hPa during the event. LWC increases along the ascent of the WCB trajectories above 900 hPa (Fig. 4). ~~This production of supercooled liquid water (SLW)~~ The increase in LWC in supercooled conditions is likely a result of (i) condensation on the water droplets advected from below to above freezing level and (ii) nucleation of new droplets at subfreezing temperatures. To maintain mixed-phase conditions, the depletion of liquid water by the Wegener–Bergeron–Findeisen process has to be compensated by production of liquid water by dynamical processes (e.g. advection of water droplets or condensation/nucleation in ascending air masses). Following this criteria, Heymsfield (1977) showed that for an ascending motion to maintain liquid water, the velocity of ascent has to be greater than a critical vertical velocity~~w_c. Korolev and Mazin (2003) showed that w_c can be expressed as a function of pressure, temperature, number concentration and mean size of ice crystals. To show that the ascent rate of the WCB is large enough to produce SLW, we estimated w_c from Fig. 10 in Korolev and Mazin (2003). If the velocity of ascent is greater than w_c, both droplets and ice particles grow.~~ . We found that in this event a vertical velocity greater than ~~0.01~~ 0.1 $\mathrm{m\,s^{-1}}$ would form supercooled droplets in the presence of both ice and snow particles (see Appendix A for details of the computation). The ascent rate of the WCB can be estimated from Fig. 4 to 0.2 $\mathrm{m\,s^{-1}}$. We conclude that the simulated SLW is a consequence of the strong large-scale ascent in the WCB. ~~To generalise this result, even the slowest WCB ascent rates of 600 in 2 days ≈ 0.05 (Wernli and Davies, 1997; Madonna et al., 2014) would be enough to maintain liquid water droplets to temperatures of -35 (Korolev and Mazin, 2003) in the conditions of this study. Since WCBs often feature higher vertical velocities (e.g. Madonna et al., 2014; Martínez-Alvarado et al., 2014; Rasp et al., 2016; Oertel et al., 2019a), we conclude that the large-scale ascent in mid-latitude wintertime WCBs is generally large enough to produce SLW.~~

4 The evolution of clouds and precipitation over Pyeongchang

In the previous section, we identified SLW associated with large-scale WCB ascents in IFS analyses. In the following, we use remote and in situ observations to corroborate the presence of SLW and to discuss its relevance for the microphyisical processes taking place.

Before the onset of precipitation, a temperature inversion at 1500 m (Fig. 6a at 00:00 UTC) favours the formation of a low-level cloud (Fig. 5a). This temperature inversion is located just above a layer of potential instability with equivalent potential temperature (θ_e) gradients of about -10 $\mathrm{K\,km^{-1}}$ between 1250 and 1450 m. Other layers of potential instability are present below 3000 m (with θ_e-gradients up to -5 $\mathrm{K\,km^{-1}}$) for all three radiosoundings at 00:00, 06:00 and 09:00 UTC. Above 3000 m, the air is saturated or close to saturation with respect to ice (Fig. 6b at 0000 UTC). At 06:00 and 09:00 UTC, the air is saturated with respect to ice over almost the entire troposphere. Between 6000 and 9000 m, the relative humidity with respect to ice (RHi) is well above ~~110~~ saturation at 00:00, 06:00 and 09:00 UTC. This altitude range corresponds to the outflow of WCB air-masses (Fig. 4), which often features cirrus clouds (Madonna et al., 2014). These cirrus in the WCB outflow are likely composed of both ice crystals formed by freezing of liquid droplets in the WCB ascent and ice crystals formed via nucleation directly from the vapour phase in upper tropospheric air masses pushed upwards by the WCB (Wernli et al., 2016). This suggests that the high supersaturation with respect to ice above 6000 m is directly related to the WCB. In this view, the WCB provides favourable conditions for rapid crystal growth leading to precipitation onset. The profile of wind speed clearly shows a strong jet of 45 $\mathrm{m\,s^{-1}}$ at 6500 m a.s.l. at 06:00 UTC (Fig. 6c), which coincides with the WCB air masses. The height of this jet and the lower limit of WCB air masses decrease with time and we observe the jet just below 5000 m at 09:00 UTC. In the layer from 4000 to 6000 m a.s.l. at 06:00 UTC an increase of wind speed with height and a rapid change of the wind direction from southerly to south-westerly result in strong vertical wind shear. The vertical wind shear reaches values of 15 $\mathrm{m\,s^{-1}\,km^{-1}}$ in speed and 0.27 $^\circ\mathrm{m^{-1}}$ in direction. Keppas et al. (2018) identified similar values of vertical wind shear, which triggered Kelvin-Helmholtz instabilities. In Sect. 5.3, we illustrate the influence of this vertical wind shear within the WCB ascent region on the observed microphysics.

Figure 5a shows the reflectivity measured by WProf. The nimbostratus cloud is approaching between 00:00 and 03:00 UTC. The cloud base is at 3100 m (Fig. 6b), but virgas appear down to 2000 m where ice crystals sublimate in unsaturated air. Below the temperature inversion at 1400 m the air is close to saturation (Fig. 6a,b at 00:00 UTC) and a low level cloud can be identified as a layer with reflectivity values below -5 dBZ. At 03:00 UTC surface precipitation starts and lasts until 16:00 UTC (Fig. 5e). A 3D gridding of the WCB trajectory positions (Fig. 5,a,b black contour) reveals that WCB air parcels are continuously ascending above the location of WProf during the entire passage of the nimbostratus cloud. At 19:00 UTC a post-frontal precipitating system sets in and lasts until 00:00 UTC 01 March. It is not associated ~~to~~ with the WCB and will not be investigated.

Within the WCB ascent regions, enhanced updraughts are present, in particular around 3000 m a.s.l. between 07:00 and 10:00 UTC (Fig. 5b). These overturning cells at the lower boundary of the WCB (represented by the black contour) are likely Kelvin-Helmholtz instabilities generated by the strong vertical wind shear observed in the radiosoundings (Fig. 6). Except for a moist neutral layer around 4000 m at 06:00 UTC, the profiles at 06:00 and 09:00 have a stable lapse rate, which together with a strong wind shear provide favourable conditions for Kelvin-Helmholtz instabilities. A region of enhanced positive Doppler velocity can be observed from 07:30 to 08:00 UTC between 4000 and 6000 m where the mean Doppler velocity amounts to approximately 2 $\mathrm{m\,s^{-1}}$, indicating the presence of embedded ~~convection~~ updraughts in the WCB. Recently, case studies by ~~Keppas et al. (2018); Oertel et al. (2019a) and Oertel et al. (2019b) also~~ Keppas et al. (2018), Oertel et al. (2019a) and Oertel et al. (2019b) identified embedded convection within the large-scale WCB. ~~Oertel et al. (2019a, b)~~ Oertel et al. (2019a) and Oertel et al. (2019b) showed that embedded convection leads to a local increase in precipitation intensity, while Oertel et al. (2019b) found that it also promotes the formation of graupel particles in the model simulations. Finally, Hogan et al. (2002) observed that embedded convection was collocated with maxima of SLW concentration. In this paper we will refer to these upwards air motions as embedded updraughts, since there is no evidence of convective instability in the radiosoundings (Fig. 6a). While the cause of the updraughts we observe might be different than those mentioned in Hogan et al. (2002); Keppas et al. (2018); Oer , the consequence on precipitation growth processes is consistent with what we observe in this study.

Ahead of the precipitating system the cloud contains mainly crystals (Fig. 5c). Starting from 04:30 UTC the intense precipitation begins and aggregates dominate during the whole precipitation period. Rimed particles are also present, especially between 06:00 and 08:00 UTC when the proportion and vertical extent of rimed particles are the largest.

The brightness temperature measured by the radiometer (Fig. 5d) is ~~a good proxy for the~~ the primary variable used to estimate the liquid water path ~~. A maximum is~~ (e.g. Küchler et al. 2017). In this study, we will use the brightness temperature as an indicator of the temporal evolution of the total liquid water in the atmospheric column. The maxima of brightness temperature observed when precipitation starts ~~at 03~~just before 04:00 UTC and ~~multiple peaks~~ the peak at 06:00 UTC corresponding to the local maximum of precipitation rate (Fig. 5e), are probably due to the partial melting of hydrometeors, since the temperature at MHS is above 0 °C. The multiple peaks after 07:00 UTC (temperature drops below freezing), which are co-occurring with updraughts, ~~suggesting~~ suggest that the updraughts favour the production of SLW in addition to the SLW produced by the large-scale ascent in the WCB. There was unfortunately no CALIPSO (satellite onboard lidar) overpass to ascertain the presence of SLW during the event. There is a local maximum in the precipitation rate just after 06:00 UTC both at MHS and GWU (Fig. 5e), while the absolute maximum is about 12 $\mathrm{mm\,h^{-1}}$ at 09:40 UTC in MHS and 13 $\mathrm{mm\,h^{-1}}$ at 14:25 UTC in GWU. Except for the maximum at 14:25 UTC in GWU and the fact that precipitation occurred from 20:00 to 23:59 UTC in MHS but not in GWU, the temporal evolution of precipitation at both locations is very similar. Note that the surface warm front never reached Pyeongchang (only the precipitation associated ~~to~~ with it), but moved further to the east. Hence, the surface temperature did not increase, in contrast to the temperature in the mid-troposphere, which increased by approximately 5 to 10 $^\circ\mathrm{C}$ (Fig. 6a) during the event.

5 Microphysial analysis of periods of interest

In the previous section we analysed the evolution of the dynamics and microphysics of the nimbostratus and precipitation associated ~~to~~ with the warm front. In this section, we will analyse succeeding periods that reveal the link between the temporal evolution of the WCB and the microphysics over Pyeongchang. Based on the homogeneity of the dominant microphysical processes, three different periods were selected: we first investigate the period dominated by depositional growth of crystals (Sect. 5.1) and subsequently analyse the effect of embedded ~~convection~~ updraughts on aggregation and riming (Sect. 5.2). Finally, we consider the impact of vertical wind shear and turbulence on aggregation (Sect. 5.3).

5.1 Vapour deposition: 03:00 to 04:00 UTC

The period from 03:00 to 04:00 UTC is dominated by crystals above 2000 m (Fig. 5c). At this time Pyeongchang is located ahead of the warm front. The vertical profiles of polarimetric variables (Fig. 7) show an increase of Z_H of ~~3~~ 2 dBZ from 6000 m to 2000 m, while Z_{DR} is almost constant from 6000 m to 3000 m, and then subsequently decreases slightly. This likely indicates the onset of aggregation at 3000 m, below which temperatures are greater than -10 $^\circ\mathrm{C}$ and hence represent favourable conditions for aggregation (Hobbs et al., 1974). K_{dp} values are almost zero, suggesting that the number concentration of oblate crystals is low. In summary, this period is characterised by the presence of crystals in limited concentration, which grew by vapour deposition and likely aggregated below 3000 m.

The selection of snowflake images (Fig. 8~~a~~b, collected at an average temperature of 1.5 $^\circ\mathrm{C}$) mainly shows small aggregates and crystals of about 2 mm in their maximum dimension. They are partly melted (liquid water is less reflective than ice and creates the dark areas on the snowflake pictures) and riming is indicated by the brighter areas. The size distribution shows that most particles are below 5 mm in size with a median of 2.2 mm. The classification shows that ~~53~~ 64 % of the observed hydrometeors are aggregates~~and 8 are crystals (sum of PC, CC and CPC). While~~, while above 2000 m, the MXPol hydrometeor classification shows predominantly ice crystals ~~are classified~~ (Fig 5c)~~, the MASC identifies the dominance of aggregates (Fig. 8b). This support~~. This supports our previous conclusion that below 3000 m, when temperature increases and aggregation is more efficient, a large fraction of crystals aggregate. ~~9~~ 7 % of particles were identified as graupel (Fig. 8b), which we could confirm by a visual analysis. Again the riming could have taken place below 2000 m, which explains why no rimed particles are present from 03:00 to 04:00 UTC in the MXPol hydrometeor classification of Fig. 5c. ~~The riming is also supported by the peak in brightness temperature from 03:00 to 04:00 UTC~~Figure 9a shows the distribution of the riming index (0=no riming, 1=graupel, Praz et al. 2017). The mode around one corresponds to the graupel particles, while half of the particles had a riming index smaller than 0.4. This shows that except for the few graupel particles, the other hydrometeor classes did not feature significant riming in comparison with other periods of the event.

5.2 Embedded ~~convection~~updraughts, riming and aggregation: 06:00 to 08:00 UTC

The period from 06:00 to 08:00 UTC is characterised by embedded ~~convection~~ updraughts (Fig. 5b), a layer with strong vertical wind shear at 3800 m (Figs. 6c,d) and significant riming, as seen by MXPol (Fig. 5c). From 6000 m to 4800 m the crystals are growing by vapour deposition leading to an increase in both Z_H and Z_{DR} (Fig. 10) as particles grow mainly along their longest dimension leading to larger and more oblate crystals (Schneebeli et al., 2013; Andrić et al., 2013; Grazioli et al., 2015). The median of K_{dp} increases to only 0.4 $^\circ\,\mathrm{km}^{-1}$, suggesting that the number concentration of oblate particles is small. Temperature ~~and ice supersaturation~~ in this layer ~~vary~~ varies from -23 $^\circ$C to -16 $^\circ$C and ~~1 to 5 respectively~~ the air is slightly above saturation with respect to ice (Fig. 6a,b). This represents favourable conditions for depositional growth of sectored plates (Lohmann et al., 2016, Fig. 8.15), while aggregation is unlikely to dominate within this temperature range according to Hobbs et al. (1974). However, we can not rule out the formation of early aggregates, which at this stage would be oblate, and hence contribute to the increase in Z_{DR} (Moisseev et al., 2015).

At 4800 m we observe a peak and subsequent decrease in Z_{DR}, which marks the end of growth dominated by vapour deposition. We hypothesise that aggregation starts at this altitude. First, after aggregation snowflakes tend to be less oblate and less dense, which explains the decrease in Z_{DR}. Second, aggregation increases the size of snowflakes, and hence Z_H continues to increase.

The observed increase in K_{dp} below the peak in Z_{DR} is a commonly observed, but not fully understood feature. Andrić et al. (2013) proposed that secondary ice generation of small oblate crystals could explain the observed enhanced K_{dp} values. Concentration of secondary ice particles can be much larger than the number of snowflakes they originate from, which would affect K_{dp} more strongly than Z_{DR} since the former is more sensitive to concentration. Moisseev et al. (2015) suggested that it is the result of the onset of aggregation, producing early aggregates that are relatively oblate. Our hypothesis is that ~~firstly,~~ first, the generation of secondary ice by droplet shattering (Mason and Maybank, 1960) and ice-ice collisions (Vardiman, 1978; Takahashi et al., 1995; Yano and Phillips, 2011) contributes to the increase in K_{dp} below 5000 m a.s.l. Droplet shattering shows a maximum of occurrence at -17 $^\circ$C (Leisner et al., 2014), which corresponds to the altitude where LWC is converted into IWC (Fig. 4 around 5000 m asl). Secondary ice generation by ice-ice collision is most effective at -15 $^\circ$C (Takahashi, 1993) and may also take place at around 5000 m a.s.l. Second, riming of already oblate crystals will tend to increase K_{dp}, because in the early stage of riming the cavities in the crystals are filled, increasing the density (and thus the dielectric response) of the hydrometeors without changing their aspect ratio. Third, rime splintering by the Hallett-Mossop process (Hallett and Mossop, 1974) below 2500 m a.s.l. (temperature above -8 $^\circ$C) can contribute to maintain high K_{dp} values. Finally, Korolev et al. (2019) recently suggested that secondary ice produced by shattering of freezing droplets transported above the melting layer could be lifted to higher levels. This may enhance the concentration of secondary ice in regions of strong updraughts. Note that the higher K_{dp} values compared to the period 03:00–04:00 UTC is primarily due to the increase of precipitation intensity, but the fact that K_{dp} increases below the onset of aggregation cannot be explained by precipitation intensity only, since aggregation decreases the number concentration and the oblateness of the particles. Riming will initially increase K_{dp} by first filling cavities and hence increasing the density of particles, but will later lead to a decrease in K_{dp} as the rime mass will smooth the particles' shape. There has to be a mechanism which produces a high number concentration of oblate particles to explain an increase in K_{dp} in a layer dominated by aggregation and riming and secondary ice production is a good candidate.

At 3800 m a strong vertical wind shear in the lower part of the WCB (black contour in Fig. 5a,b,c at 06:00 UTC) can be observed in both the radiosoundings (Fig. 6c,d) and the spectral width profiles (Fig. 10). The jet at 6500 m at 06:00 UTC (Fig. 6c) can be seen as an enhancement of Doppler velocity between 4000 and 6000 m a.s.l. with a maximum of 45 $\mathrm{m\,s^{-1}}$ at 5000 m in the RHI of Fig. 11. This is in good agreement with the wind speed measured by the radiosonde at 06:00 UTC, since the RHI is almost aligned with the wind direction. The vertical wind shear at 3800 m is visible as the Doppler velocity decreases in the lower part of the WCB and reaches a value of 0 $\mathrm{m\,s^{-1}}$ at 3000 m (combined effect of a decrease in wind speed and change of wind direction from parallel to perpendicular to the radar beam). This vertical wind shear may generate Kelvin-Helmholtz instabilities, which can trigger embedded convection (Hogan et al., 2002). Moreover ~~the layers of potential instability below 3000 (Fig. 6a) indicate that instability can be released, if sufficient lifting is provided, for instance by the Kelvin-Helmholtz waves. Finally,~~ orography might also play a role in lifting the easterly low-level flow, which directly impinges the Taebaek mountains from the East Sea. These sources of lifting together with the ~~potential instability~~ moist neutral layers below 3000 m (Fig. 6a) can lead to the observed strong updraughts (Fig. 5b), which promote aggregation by increasing the probability of collisions between particles. The effect of turbulent cells on aggregation has been discussed thoroughly in ~~Houze and Medina (2005); Medina et al. (2005); Medina and Houze (2015)~~Houze and Medina (2005), Medina et al. (2005) and Medina and Houze (2015). Houze and Medina (2005) suggested that overturning cells promote both aggregation and riming. First, they can sustain the production of SLW necessary for riming. Second, the turbulence increases the probability of collision between particles. Finally, aggregates are larger targets for the collection of SLW droplets, which again enhances growth by riming. While the cause of the turbulence is different here, the processes described are consistent with our measurements.

The MASC images (Fig. 12a) show mainly rimed aggregates of about 10 mm in their maximum dimension and two graupel particles. The average temperature of collection was 0.1 $^{\circ}\mathrm{C}$ and hence the particles should not be as melted as during the period 03:00–04:00 UTC. The classification shows a majority of aggregates (~~61~~ 77 %). The hydrometeor classification from Besic et al. (2018) classifies rimed aggregates and graupel as rimed particles, whereas the MASC based classification from Praz et al. (2017) classifies only fully rimed particles as graupel and the aggregates class contains also rimed aggregates. Therefore a direct comparison of the class aggregates between the two classification methods is difficult. The size distribution is much broader than from 03:00 to 04:00 UTC with particles reaching 13 mm in their maximum dimension. The median amounts to 2.8 mm, as there is still a significant proportion of small particles. The total number of particles is ~~1212~~2589, while it was ~~131~~ 55 in the previous period, showing that this period features more intense precipitation, which also makes the empirical size distribution more robust. The 75th percentile is 4.7 mm compared to 3.0 mm for the period 03:00 to 04:00 UTC, showing that the particles from 06:00 to 08:00 UTC are significantly larger. These large rimed aggregates can be attributed to the strong updraughts, which enhance the growth by aggregation and riming. Note that while the previous period (Sec. 5.1) featured riming below 2000 m, the precipitation rate was much smaller than from 06:00 to 08:00 UTC (Fig. 5e) and hence this riming did not contribute significantly to the total precipitation accumulation. The important message here is that the flow conditions in the WCB promoted rapid precipitation growth by aggregation and riming above 2000 m and are thus responsible for the large precipitation accumulation between 06:00 to 08:00 UTC. Moreover, most of the particles have higher quartiles of riming index (Fig. 9b) than between 03:00 to 04:00 UTC, despite the lower proportion of graupels, which is due to the enhanced aggregation favouring rimed aggregates at the expense of pure graupel. We conclude that this period features the most riming, both in absolute mass and in relative terms over all hydrometeor classes.

Figure 13 shows a range spectrogram from WProf averaged from 07:42 UTC to 07:47 UTC and from 07:57 UTC to 08:02 UTC. The updraught present in Fig. 5b can be seen as a strong shift in the mode of the spectrum from about -0.5 $\mathrm{m\,s^{-1}}$ at 6000 m to above 2 $\mathrm{m\,s^{-1}}$ at 5000 m (Fig. 13a). This updraught goes along with strong turbulence which is visible as an increase in spectral width between 4000 m and 6000 m. By 07:57 UTC (Fig. 13b), the increase ~~of reflectivity and~~ in spectral reflectivity together with a decrease in Doppler velocity from 4800 to 4000 m ~~suggest~~ suggests that large aggregates likely formed in the turbulent layer and further aggregate during their fall. This is consistent with the onset of aggregation below 5000 m observed in Fig. 10. The enhanced aggregation in the updraughts present from around 07:30 UTC to 08:00 UTC leads to an increase of precipitation rate from 07:55 UTC to the maximum at 09:40 UTC (Fig. 5e). ~~This corresponds to aggregates that were formed in the updraughts present from around 07:30 UTC to 08:00 UTC.~~ Particles that started falling between 4000 and 5000 m will take ~~about~~ 85–105 min to fall to the ground with an average effective fall speed (absolute fall speed plus updraught) of 0.8 $\mathrm{m\,s^{-1}}$. This is consistent with the increase in precipitation intensity from 07:55 to 09:40 UTC and the maximum could correspond to aggregates that formed in the updraught between 07:35 to 07:55 UTC. This hypothesis assumes a certain horizontal homogeneity, supported by the increase in precipitation in both rain gauge measurements in MHS and GWU that are separated by 19 km (Fig. 5e). It would imply that the embedded ~~convection is~~ updraughts are responsible for the period of strongest precipitation, which also features intense riming (Fig. 5c), consistent with the suggestion in Oertel et al. (2019a, b).

~~Figure ?? shows a time spectrogram from 07:31 UTC to 08:01 UTC at 5000 . Updraughts start at 07:36 UTC and reach maxima of 2.5 between 07:41 UTC and 07:46 UTC. During this period, significant aggregation increases the reflectivity values as particles get larger, which, combined with a decrease in the updraught speed, lowers the mean Doppler velocities and some particles start to fall at 07:51 UTC. Hence, the particles were suspended during 15 in heavy turbulent conditions, showing that updraughts also promote aggregation by increasing the time hydrometeors have to aggregate.~~

5.3 Shear-induced turbulence: 09:00 to 11:00 UTC

The period from 09:00 to 11:00 UTC features turbulence and intense precipitation rates (Fig. 5b, e). Due to a malfunction of the MASC, only pictures between 10:08 and 10:50 UTC were collected, leading to only ~~286~~ 69 particles during this period (Fig. 14). There are substantially more crystals (~~31~~ 10 %) ~~and graupel particles~~ than during the other periods. Figure 14a shows a few small aggregates, columnar and planar crystals and one graupel. The median of the size distribution is at 2.7 mm, and the 75th and 95th percentiles are at 3.9 mm and 6.6 mm, respectively, indicating that the particles are smaller than in the previous period. Figure 15 shows a less pronounced increase in Z_{DR} compared to the period between 06:00 to 08:00 UTC (Fig. 10), suggesting that the depositional growth rate is smaller than during the previous period. The median of Z_{DR} increases to 0.7 dB around 4200 m, where crystals and aggregates probably dominate. The median of Z_H reaches a maximum of 22 dBZ at 2000 m, compared to 25 dBZ at 06:00–08:00 UTC (Fig. 10). This is consistent with the size distribution (06:00–08:00 UTC in Fig. 12) that shows more large particles than Fig. 14. Below 4200 m, larger aggregates start to form as temperatures exceed -15 $^\circ\mathrm{C}$ and Z_{DR} decreases slightly. It is collocated with the increase in spectral width (Fig. 15), reflecting the vertical wind shear below the maximum wind speed (6c) at 09:00 UTC. The shear layer was between 4000 and 5000 m in the period from 06:00 to 08:00 UTC, while it is now between 3000 m and 4000 m. This vertical wind shear is collocated with the turbulent cells observed in Fig. 5b from 08:00 to 10:00 UTC around 4000 m, which suggests that they originate from Kelvin-Helmholtz instabilities. This is supported by values of the gradient Richardson number (not shown here) of 0.2 where the turbulent cells are present. The decrease in the height of the wind shear is consistent with the decrease in the height of maximum wind speed between 06:00 and 09:00 UTC (Fig. 6c), and explains why the altitude of aggregation enhancement by turbulence decreases with time. This was also observed by Keppas et al. (2018), who attributed this altitude decrease of the maximum of wind speed to the passage of the warm front. On the other hand, the altitude of the onset of aggregation could increase with time as the warm front passes, because the altitude of the -15 $^\circ\mathrm{C}$ isotherm [relative maximum of aggregation in Hobbs et al., 1974] is higher at 09:00 UTC than at 06:00 UTC. Our interpretation is that the enhancement of aggregation by turbulence dominates the polarimetric signatures in our case. First, because crystals were likely growing as sectored plates and not as dendrites, the latter being more effective to aggregate at -15 $^\circ\mathrm{C}$. Second, the intense aggregation taking place in the shear layer leads to larger aggregates than the early aggregation at -15 $^\circ\mathrm{C}$, which makes the former more visible in the polarimetric profiles. The distribution of the riming index (Fig. 9c) is broader than for the other periods due to the higher proportions of crystal-like particles and the presence of graupel and rimed aggregates.

6 A conceptual model

The findings of this case study can be summarised in a conceptual model (Fig. 16). As the WCB rises from the boundary layer, the air saturates and the liquid water droplets eventually become supercooled. If the ascent rate is strong enough (which is the case for most WCBs, see Sect. 3), SLW can be produced and persist to the mid-troposphere. Crystals grow by vapour deposition at upper levels of the WCB ascent (see RHi $> 110\,\%$ in Fig. 6b) leading to an increase in Z_H and Z_{DR}. During their fall, they experience riming by accretion of supercooled droplets. Moreover, the vertical wind shear (large SW) at the lower-boundary of the WCB creates turbulence, which enhances aggregation by increasing the probability of collisions between hydrometeors. Furthermore, embedded ~~convection~~ updraughts in the WCB (as seen by positive vertical Doppler velocities) can additionally lift precipitating particles and increases their time for growth by aggregation. Finally, aggregates are larger targets for collection of SLW, which enhances riming. This leads to large rimed aggregates and local peaks in precipitation intensity. In the layer of growth by aggregation and riming, Z_H increases, while Z_{DR} decreases. Additionally, generation of secondary ice by droplet shattering and ice-ice collision leads to an increase in K_{dp}. In the outflow region of the WCB, crystals, which either formed by nucleation from the vapour phase or freezing of the remaining supercooled droplets, fall and may aggregate without significant riming. While this conceptual model is built upon a single case study, we postulate that the key processes, which are production of SLW and turbulence enhancing riming and aggregation, can take place in most wintertime mid-latitude cyclones featuring a strong WCB.

7 Conclusion

This study investigates the snowfall microphysics associated ~~to~~ with a WCB during an extreme wintertime precipitation event in South Korea. We combined Doppler dual-polarisation radar measurements, snowflake photographs, radiosonde data with IFS data and trajectories to characterise the detailed precipitation growth mechanisms associated with the large-scale WCB ascent.

The main findings can be summarised as follows:

- We identified a WCB in IFS analyses as rapidly ascending air masses (approximately 600 hPa in 12 h) in the vicinity of Pyeongchang. A strong jet and enhanced vertical wind shear within the WCB ascent region are clearly visible in radiosonde data and Doppler velocity measurements from MXPol.

- The IFS analyses show that SLW (up to 0.2 $\mathrm{g\,kg^{-1}}$) is produced during the rapid ascent in the WCB by condensation of water vapour. In agreement with IFS analyses, multiple peaks in the brightness temperature of the radiometer during the passage of the warm front corroborate the presence of SLW. The timing and presence of SLW is additionally confirmed by the presence of rimed particles observed by the MASC and a hydrometeor classification based on MXPol data.

- The vertical wind shear promotes aggregation and riming by producing SLW, updraughts and turbulence, which enhance the probability of collisions between particles.

- Three periods could be identified, where the governing microphysical processes are directly influenced by the specific flow conditions in the WCB. In the first period, Pyeongchang is located below the WCB outflow (Fig. 5a). No strong updraughts were present, the precipitation intensity was low and we observed mainly small aggregates and crystals. In the second and third periods, Pyeongchang is located below WCB ascent. A layer with strong vertical wind shear, whose height decreases with time, generates turbulent cells and updraughts. The precipitation intensity peaks between 7 and 10 $\mathrm{mm\,h^{-1}}$ and large rimed aggregates are observed.

This study enabled the investigation of the impact of a large-scale feature, such as a WCB, on the microphysics thanks to the complementarity of atmospheric models, remote-sensing and in situ measurements. It suggests a strong coupling between processes on the synoptic and micro-scales that has to be assessed when evaluating the representation of cloud and precipitation in atmospheric models. While this case study presents a detailed analysis of field measurements, additional investigations with in situ measurements in clouds - characterising the presence of SLW for instance - are needed to further constrain and evaluate the coupling between large-scale dynamical processes and microphysics in models.

Code and data availability. The trajectories were computed with the Lagrangian analysis tool LAGRANTO (Sprenger and Wernli, 2015). We used functions from the Python libraries Py-ART (Helmus and Collis, 2016) and MetPy (May et al., 2008). Other codes and data are available upon request to the corresponding author.

Appendix A: Estimation of the critical vertical velocity

In this appendix we will show details on the estimation of the critical vertical velocity U_z^* needed to form and maintain liquid water in the presence of both ice crystals and snow. Korolev and Mazin (2003) showed that U_z^* can be expressed as a function of pressure, temperature, number concentration and mean size of ice crystals. We use Fig. 10 in Korolev and Mazin (2003), which gives the relation between U_z^* and the product of the number concentration of ice particles N_i and the characteristic size of ice particles r_i for temperature between -35°C and -5°C. Since in our case we have both ice and snow particles, we compute separately N_i and the number concentration of snow particles N_s such that the total number concentration is: $N_{tot} = N_i + N_s$. We also compute the characteristic size of the mixture of ice and snow particles r_{tot}. The expression for N_i is given by Eq. 7.40 of ECMWF (2016):

$$N_i = 100\,exp[12.96\,(e_{sl} - e_{si})/e_{si} - 0.639], \tag{A1}$$

where e_{sl} (e_{si}) is the saturation vapour pressure with respect to liquid (ice). The expression for N_s is given by Eqs. 7.15 to 7.19 in ECMWF (2016). In our case it is simply expressed by:

$$N_s = \Lambda^{-1} N_{0s}, \tag{A2}$$

where $N_{0s} = n_{as} = 2 \cdot 10^6$ (Eq. 7.16 and Table 7.1 of ECMWF (2016)) and Λ is given by (Eq. 7.18 of ECMWF 2016):

$$\Lambda = \left(\frac{n_{as} a_s \Gamma(3)}{q_s rho}\right)^{1/(b_s+1-n_{bs})} \tag{A3}$$

$$\Gamma(3) = \int_0^\infty D^2\, e^{-D}\, dD = 2, \tag{A4}$$

where $a_s = 0.069$, $b_s = 2$, $n_{bs} = 0$ are given in Table 7.1 and 7.2 of ECMWF (2016). The expression for r_i can be found by stating that the characteristic volume of an ice particle V_i is:

$$V_i = \frac{\rho q_i}{\rho_i N_i}, \quad \text{(A5)}$$

where ρ is the air density, ρ_i the density of ice particles and q_i the mixing ratio of ice. Assuming spherical particles, we can express r_i with:

$$r_i = \left(\frac{3 \rho q_i}{4 \rho_i N_i \pi}\right)^{1/3}, \quad \text{(A6)}$$

Since snow particles are spherical in IFS and considered as having the same density as ice, we have $\rho_i = \rho_s$. We define r_{tot} as:

$$r_{tot} = \left(\frac{3 \rho (q_i + q_s)}{4 \rho_i N_{tot} \pi}\right)^{1/3} \quad \text{(A7)}$$

Using the values described in Table A1, we find $N_{tot} r_{tot} = 1.7\,\mu\mathrm{m\,cm^{-3}}$, which we can use in Fig. 10 of Korolev and Mazin (2003) to read U_z^* at about -13 °C and find 0.1 $\mathrm{m\,s^{-1}}$.

Author contributions. JG and AB designed the experiment. JG operated the instruments, processed and analysed the observational data. AO computed and analysed the WCB trajectories. NJ computed the MASC size distributions. NB computed the radar based hydrometeor classification. JG, AO, EV and AB interpreted the data. JG, with contributions of all authors, prepared the manuscript.

Competing interests. The authors declare that they have no conflict of interest.

Acknowledgements. We are grateful for the support provided by the Korea Meteorological Administration and the World Meteorological Organisation making possible the ICE-POP 2018 weather research and development projects and the observational data used in this publication. In particular, we are thankful to the High Impact Weather Research Center of the Korea Meteorological Organisation for providing us with radiosonde data and giving us access to their facilities at the Gangneung Wonju National University. We would also like to thank Christophe Praz and Jacques Grandjean for their help during the deployment of the instruments. Special thanks go to KwangDeuk Ahn from the Korea Meteorological Organisation for his support during the campaign and to Kwonil Kim for his help with some instruments. Finally, we would like to thanks Hanna Joos and Heini Wernli from ETH for their review and constructive comments on the manuscript. JG and AO acknowledge the financial support from the Swiss National Science Foundation (grants 175700/1 and 165941, respectively).

References

Andrić, J., Kumjian, M. R., Zrnić, D. S., Straka, J. M., and Melnikov, V. M.: Polarimetric signatures above the melting layer in winter storms: An observational and modeling study, Journal of Applied Meteorology and Climatology, 52, 682–700, https://doi.org/10.1175/JAMC-D-12-028.1, 2013.

Bader, M. J., Clough, S. A., and Cox, G. P.: Aircraft and dual polarization radar observations of hydrometeors in light stratiform precipitation, Quarterly Journal of the Royal Meteorological Society, 113, 491–515, https://doi.org/10.1002/qj.49711347605, 1987.

Besic, N., Figueras i Ventura, J., Grazioli, J., Gabella, M., Germann, U., and Berne, A.: Hydrometeor classification through statistical clustering of polarimetric radar measurements: A semi-supervised approach, Atmospheric Measurement Techniques, 9, 4425–4445, https://doi.org/10.5194/amt-9-4425-2016, 2016.

Besic, N., Gehring, J., Praz, C., Figueras i Ventura, J., Grazioli, J., Gabella, M., Germann, U., and Berne, A.: Unraveling hydrometeor mixtures in polarimetric radar measurements, Atmospheric Measurement Techniques, 11, 4847–4866, https://doi.org/10.5194/amt-11-4847-2018, 2018.

Bringi, V. N. and Chandrasekar, V.: Polarimetric Doppler Weather Radar: Principles and Applications, Cambridge University Press, https://doi.org/10.1017/CBO9780511541094, 2001.

Browning, K. A.: Organisation of clouds and precipitation in extratropical cyclones, Amer. Meteorol. Soc., Boston, MA, 1990.

Browning, K. A., Hardman, M. E., Harrold, T. W., and Pardoe, C. W.: The structure of rainbands within a mid-latitude depression, Quarterly Journal of the Royal Meteorological Society, 99, 215–231, https://doi.org/10.1002/qj.49709942002, 1973.

Carlson, T. N.: Airflow through midlatitude cyclones and the comma cloud pattern., https://doi.org/10.1175/1520-0493(1980)108<1498:ATMCAT>2.0.CO;2, 1980.

Colle, B. a., Stark, D., and Yuter, S. E.: Surface Microphysical Observations within East Coast Winter Storms on Long Island, New York, Monthly Weather Review, 142, 3126–3146, https://doi.org/10.1175/MWR-D-14-00035.1, 2014.

Dacre, H. F., Martínez-Alvarado, O., and Mbengue, C. O.: Linking Atmospheric Rivers and Warm Conveyor Belt Airflows, Journal of Hydrometeorology, 20, 1183–1196, https://doi.org/10.1175/jhm-d-18-0175.1, 2019.

Eckhardt, S., Stohl, A., Wernli, H., James, P., Forster, C., and Spichtinger, N.: A 15-year climatology of warm conveyor belts, Journal of Climate, 17, 218–237, https://doi.org/10.1175/1520-0442(2004)017<0218:AYCOWC>2.0.CO;2, 2004.

ECMWF: IFS Documentation – Cy41r2, Part IV: Physical Processes, https://www.ecmwf.int/sites/default/files/elibrary/2016/16648-part-iv-physical-processes.pdf, last access: 16 April 2020, 2016.

ECMWF: IFS Documentation - Cy43r3: Operational implementation 11 July 2017. Dynamics and numerical procedures., 2017.

Forbes, R., Tompkins, A., and Untch, A.: A new prognostic bulk microphysics scheme for the IFS, p. 22, https://doi.org/10.21957/bf6vjvxk, https://www.ecmwf.int/node/9441, 2011.

Garrett, T. J., Fallgatter, C., Shkurko, K., and Howlett, D.: Fall speed measurement and high-resolution multi-angle photography of hydrometeors in free fall, Atmospheric Measurement Techniques, 5, 2625–2633, https://doi.org/10.5194/amt-5-2625-2012, 2012.

Grazioli, J., Lloyd, G., Panziera, L., Hoyle, C. R., Connolly, P. J., Henneberger, J., and Berne, A.: Polarimetric radar and in situ observations of riming and snowfall microphysics during CLACE 2014, Atmospheric Chemistry and Physics, 15, 13 787–13 802, https://doi.org/10.5194/acp-15-13787-2015, 2015.

Green, J. S., Ludlam, F. H., and McIlveen, J. F.: Isentropic relative flow analysis and the parcel theory, Quarterly Journal of the Royal Meteorological Society, 92, 210–219, https://doi.org/10.1002/qj.49709239204, 1966.

Hallett, J. and Mossop, S. C.: Production of secondary ice particles during the riming process, Nature, 249, 26–28, https://doi.org/10.1038/249026a0, 1974.

Harrold, T.: Mechanisms influencing the distribution of precipitation within baroclinic disturbances, Quarterly Journal of the Royal Meteorological Society, 99, 232–251, 1973.

Hawcroft, M. K., Shaffrey, L. C., Hodges, K. I., and Dacre, H. F.: How much Northern Hemisphere precipitation is associated with extratropical cyclones?, Geophysical Research Letters, 39, 1–7, https://doi.org/10.1029/2012GL053866, 2012.

Helmus, J. J. and Collis, S. M.: The Python ARM Radar Toolkit (Py-ART), a Library for Working with Weather Radar Data in the Python Programming Language, Journal of Open Research Software, 4, https://doi.org/10.5334/jors.119, 2016.

Heymsfield, A. J.: Precipitation Development in Stratiform Ice Clouds: A Microphysical and Dynamical Study, https://doi.org/10.1175/1520-0469(1977)034<0367:pdisic>2.0.co;2, 1977.

Hobbs, P. V., Chang, S., and Locatelli, J. D.: The dimensions and aggregation of ice crystals in natural clouds, Journal of Geophysical Research, 79, 2199–2206, https://doi.org/10.1029/JC079i015p02199, http://doi.wiley.com/10.1029/JC079i015p02199, 1974.

Hogan, R. J., Field, P. R., Illingworth, a. J., Cotton, R. J., and Choularton, T. W.: Properties of embedded convection in warm-frontal mixed-phase cloud from aircraft and polarimetric radar, Quarterly Journal of the Royal Meteorological Society, 128, 451–476, https://doi.org/10.1256/003590002321042054, http://dx.doi.org/10.1256/003590002321042054, 2002.

Houze, R. a. and Medina, S.: Turbulence as a Mechanism for Orographic Precipitation Enhancement, Journal of the Atmospheric Sciences, 62, 3599–3623, https://doi.org/10.1175/JAS3555.1, 2005.

Joos, H. and Forbes, R. M.: Impact of different IFS microphysics on a warm conveyor belt and the downstream flow evolution, Q. J. Roy. Meteor. Soc., 142, 2727–2739, https://doi.org/10.1002/qj.2863, 2016.

Joos, H. and Wernli, H.: Influence of microphysical processes on the potential vorticity development in a warm conveyor belt: A case-study with the limited-area model COSMO, Quarterly Journal of the Royal Meteorological Society, 138, 407–418, https://doi.org/10.1002/qj.934, 2012.

Jullien, N., Vignon, É., Reverdin, A., Praz, C., and Berne, A.: Snowfall particle size distributions at Dumont d'Urville station from MASC measurements, in: 27th IUGG Assembly, p. 1, Montréal, 2019.

Keppas, S. C., Crosier, J., Choularton, T. W., and Bower, K. N.: Microphysical properties and radar polarimetric features within a warm front, Monthly Weather Review, 146, 2003–2022, https://doi.org/10.1175/MWR-D-18-0056.1, 2018.

Korolev, A., Heckman, I., Wolde, M., Ackerman, A. S., Fridlind, A. M., Ladino, L., Lawson, P., Milbrandt, J., and Williams, E.: A new look at the environmental conditions favorable to secondary ice production, Atmospheric Chemistry and Physics Discussions, pp. 1–67, https://doi.org/10.5194/acp-2019-611, 2019.

Korolev, A. V. and Mazin, I. P.: Supersaturation of water vapor in clouds, Journal of the Atmospheric Sciences, 60, 2957–2974, https://doi.org/10.1175/1520-0469(2003)060<2957:SOWVIC>2.0.CO;2, 2003.

Küchler, N., Kneifel, S., Löhnert, U., Kollias, P., Czekala, H., and Rose, T.: A W-Band Radar–Radiometer System for Accurate and Continuous Monitoring of Clouds and Precipitation, Journal of Atmospheric and Oceanic Technology, 34, 2375–2392, https://doi.org/10.1175/JTECH-D-17-0019.1, http://journals.ametsoc.org/doi/10.1175/JTECH-D-17-0019.1, 2017.

Kumjian, M.: Principles and applications of dual-polarization weather radar. Part III: Artifacts, Journal of Operational Meteorology, 1, 265–274, https://doi.org/10.15191/nwajom.2013.0121, 2013.

Kumjian, M. R., Rutledge, S. A., Rasmussen, R. M., Kennedy, P. C., and Dixon, M.: High-resolution polarimetric radar observations of snow-generating cells, Journal of Applied Meteorology and Climatology, 53, 1636–1658, https://doi.org/10.1175/JAMC-D-13-0312.1, 2014.

Leisner, T., Pander, T., Handmann, P., and Kiselev, A.: Secondary ice processes upon heterogeneous freezing of cloud droplets, in: 14th Conf. on Cloud Physics and Atmospheric Radiation, edited by Amer. Meteor. Soc., ., Boston, MA, 2014.

Lohmann, U., Luond, F., and Mahrt, F.: An Introduction to Clouds, Cambridge Univ. Press, 2016.

Madonna, E., Wernli, H., Joos, H., and Martius, O.: Warm conveyor belts in the ERA-Interim Dataset (1979-2010). Part I: Climatology and potential vorticity evolution, Journal of Climate, 27, 3–26, https://doi.org/10.1175/JCLI-D-12-00720.1, 2014.

Martínez-Alvarado, O., Joos, H., Chagnon, J., Boettcher, M., Gray, S. L., Plant, R. S., Methven, J., and Wernli, H.: The dichotomous structure of the warm conveyor belt, Quarterly Journal of the Royal Meteorological Society, 140, 1809–1824, https://doi.org/10.1002/qj.2276, 2014.

Mason, B. J. and Maybank, J.: The fragmentation and electrification of freezing water drops, Q. J. Roy. Meteor. Soc., 86, 176–185, https://doi.org/10.1175/1520-0469(1975)032<0974:TFAEOF>2.0.CO;2, 1960.

May, R. M., Arms, S. C., Marsh, P., Bruning, E., and Leeman, J. R.: MetPy: A Python package for meteorological data, https://doi.org/10.5065/D6WW7G29, https://github.com/Unidata/MetPy, 2008.

Medina, S. and Houze, R. A.: Small-Scale Precipitation Elements in Midlatitude Cyclones Crossing the California Sierra Nevada, Monthly Weather Review, 143, 2842–2870, https://doi.org/10.1175/MWR-D-14-00124.1, http://journals.ametsoc.org/doi/10.1175/MWR-D-14-00124.1, 2015.

Medina, S., Smull, B. F., Houze, R. A., and Steiner, M.: Cross-Barrier Flow during Orographic Precipitation Events: Results from MAP and IMPROVE, Journal of the Atmospheric Sciences, 62, 3580–3598, https://doi.org/10.1175/jas3554.1, 2005.

Moisseev, D. N., Lautaportti, S., Tyynela, J., and Lim, S.: Dual-polarization radar signatures in snowstorms: Role of snowflake aggregation, Journal of Geophysical Research: Atmospheres, 120, 12 644–12 655, https://doi.org/10.1002/2015JD023884, 2015.

Oertel, A., Boettcher, M., Joos, H., Sprenger, M., Konow, H., Hagen, M., and Wernli, H.: Convective activity in an extratropical cyclone and its warm conveyor belt – a case-study combining observations and a convection-permitting model simulation, Quarterly Journal of the Royal Meteorological Society, 145, 1406–1426, https://doi.org/10.1002/qj.3500, 2019a.

Oertel, A., Boettcher, M., Joos, H., Sprenger, M., and Wernli, H.: Potential vorticity structure of embedded convection in a warm conveyor belt and its relevance for the large-scale dynamics, Weather and Climate Dynamics Discussions, pp. 1–38, https://doi.org/10.5194/wcd-2019-3, 2019b.

Pfahl, S., Madonna, E., Boettcher, M., Joos, H., and Wernli, H.: Warm conveyor belts in the ERA-Interim data set (1979-2010). Part II: Moisture origin and relevance for precipitation, Journal of Climate, 27, 27–40, https://doi.org/10.1175/JCLI-D-13-00223.1, http://journals.ametsoc.org/doi/abs/10.1175/JCLI-D-13-00223.1, 2014.

Praz, C., Roulet, Y.-A., and Berne, A.: Solid hydrometeor classification and riming degree estimation from pictures collected with a Multi-Angle Snowflake Camera, Atmospheric Measurement Techniques, pp. 1–40, https://doi.org/10.5194/amt-2016-417, http://www.atmos-meas-tech-discuss.net/amt-2016-417/, 2017.

Rasp, S., Selz, T., and Craig, G. C.: Convective and slantwise trajectory ascent in convection-permitting simulations of midlatitude cyclones, Monthly Weather Review, 144, 3961–3976, https://doi.org/10.1175/MWR-D-16-0112.1, 2016.

Rutz, J. J., James Steenburgh, W., and Martin Ralph, F.: Climatological characteristics of atmospheric rivers and their inland penetration over the western united states, Monthly Weather Review, 142, 905–921, https://doi.org/10.1175/MWR-D-13-00168.1, 2014.

Schaer, M., Praz, C., and Berne, A.: Identification of blowing snow particles in images from a multi-angle snowflake camera, The Cryosphere Discussions, pp. 1–23, https://doi.org/10.5194/tc-2018-248, 2018.

Schneebeli, M., Dawes, N., Lehning, M., and Berne, A.: High-resolution vertical profiles of X-band polarimetric radar observables during snowfall in the Swiss Alps, Journal of Applied Meteorology and Climatology, 52, 378–394, https://doi.org/10.1175/JAMC-D-12-015.1, 2013.

Schultz, D. M.: Reexamining the cold conveyor belt, Monthly Weather Review, 129, 2205–2225, https://doi.org/10.1175/1520-0493(2001)129<2205:RTCCB>2.0.CO;2, 2001.

Sprenger, M. and Wernli, H.: The LAGRANTO Lagrangian analysis tool - Version 2.0, Geoscientific Model Development, 8, 2569–2586, https://doi.org/10.5194/gmd-8-2569-2015, 2015.

Takahashi, T.: High ice crystal production in winter cumuli over the Japan Sea, Geophysical Research Letters, 20, 451–454, https://doi.org/10.1029/93GL00613, 1993.

Takahashi, T., Yoshihiro Nagao, and Kushiyama, Y.: Possible High Ice Particle Production during Graupel–Graupel Collisions, American Meteorological Society, 52, 4523–4527, 1995.

Vardiman, L.: The Generation of Secondary Ice Particles in Clouds by Crystal–Crystal Collision, https://doi.org/10.1175/1520-0469(1978)035<2168:tgosip>2.0.co;2, 1978.

Wernli, H. and Davies, H. C.: A Lagrangian-based analysis of extratropical cyclones. I: The method and some applications, Quarterly Journal of the Royal Meteorological Society, 123, 467–489, https://doi.org/10.1256/smsqj.53810, 1997.

Wernli, H. and P., K.: WCBs and TMEs and Their Relationship to ARs, in: Atmospheric Rivers, edited by Ralph, F., Dettinger, M., Rutz, J., and Waliser, D., chap. 3.2, pp. XX, 366, Springer International Publishing, https://doi.org/10.1007/978-3-030-28906-5, 2020.

Wernli, H. and Schwierz, C.: Surface Cyclones in the ERA-40 Dataset (1958–2001). Part I: Novel Identification Method and Global Climatology, Journal of the Atmospheric Sciences, 63, 2486–2507, https://doi.org/10.1175/JAS3766.1, http://journals.ametsoc.org/doi/abs/10.1175/JAS3766.1, 2006.

Wernli, H., Boettcher, M., Joos, H., Miltenberger, A. K., and Spichtinger, P.: A trajectory-based classification of ERA-Interim ice clouds in the region of the North Atlantic storm track, Geophysical Research Letters, 43, 6657–6664, https://doi.org/10.1002/2016GL068922, 2016.

Yano, J.-I. and Phillips, V. T. J.: Ice–Ice Collisions: An Ice Multiplication Process in Atmospheric Clouds, Journal of the Atmospheric Sciences, 68, 322–333, https://doi.org/10.1175/2010JAS3607.1, http://journals.ametsoc.org/doi/abs/10.1175/2010JAS3607.1, 2011.

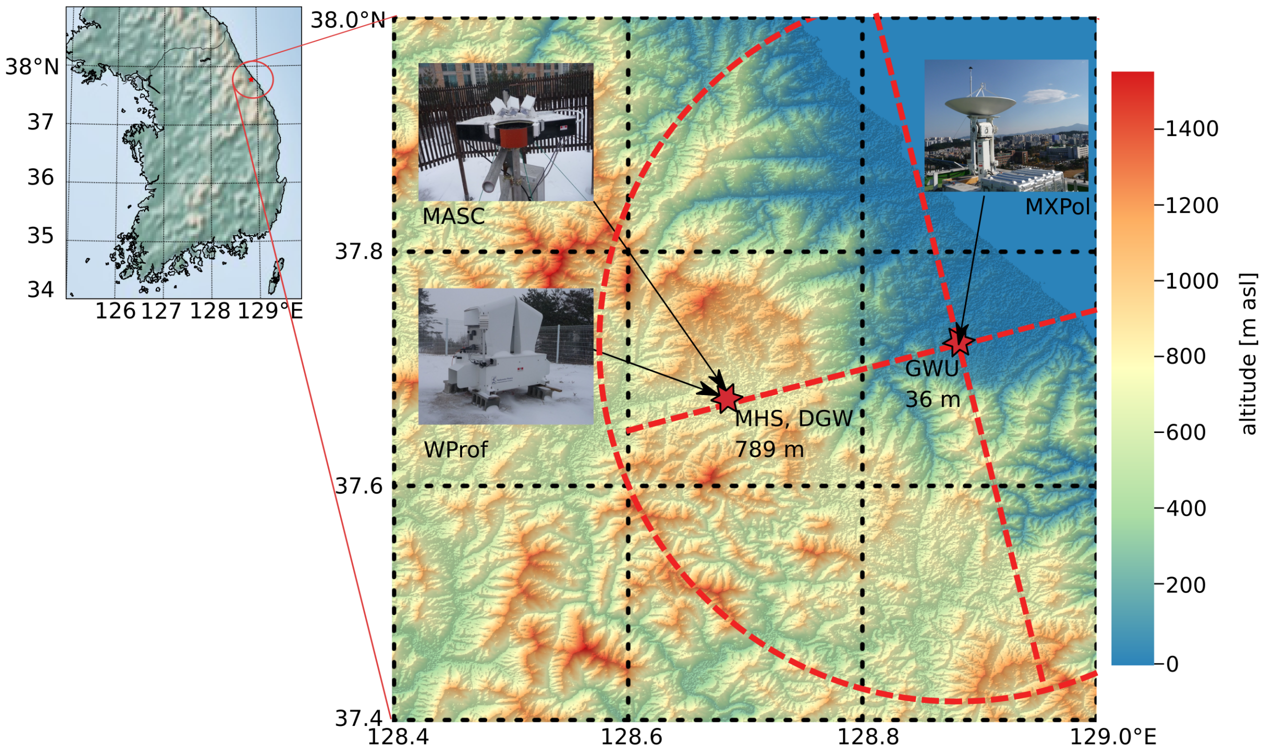

Figure 1. Location of the main measurements sites of ICE-POP 2018 used in this study. A digital elevation model shows the topography of the region and its location within South Korea. The red dotted lines and circle show the extent of the main RHIs (27.2 km) and PPI (28.4 km radius) respectively.

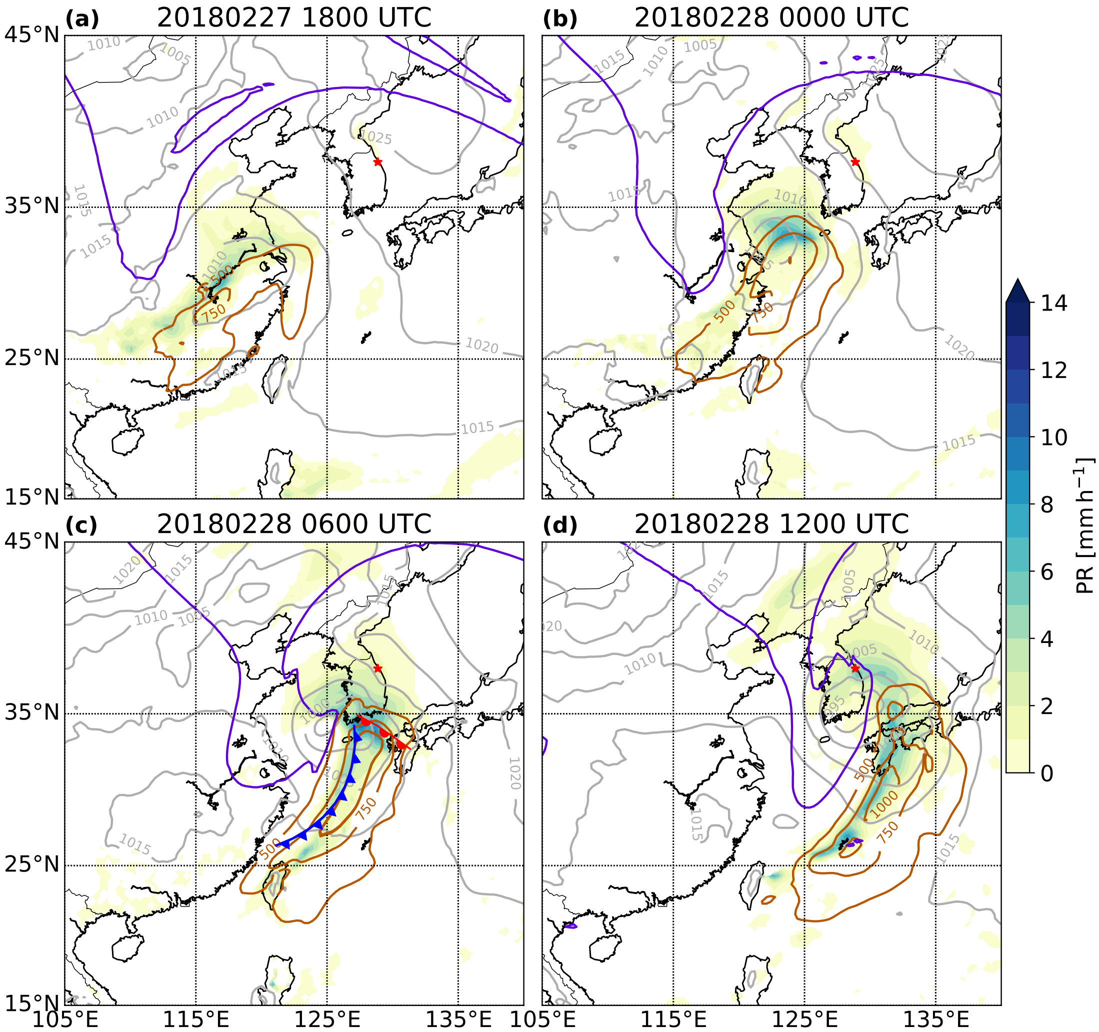

Figure 2. Sea level pressure (grey contours, labels in hPa), dynamical tropopause on the 315 K isentrope (purple line), IVT (brown contours, labels in $\mathrm{kg\,m^{-1}\,s^{-1}}$, only values greater than 500 $\mathrm{kg\,m^{-1}\,s^{-1}}$ are shown), precipitation rate (PR) in $\mathrm{mm\,h^{-1}}$ (colour filled) at (a) 18:00 UTC 27 February 2018 (b) 00:00 UTC, (c) 06:00 UTC, (d) 12:00 UTC 28 February 2018 from ERA5 data. The warm and cold fronts at 06:00 UTC were manually drawn based on an analysis of equivalent potential temperature on 850 hPa. The red star shows the location of GWU.

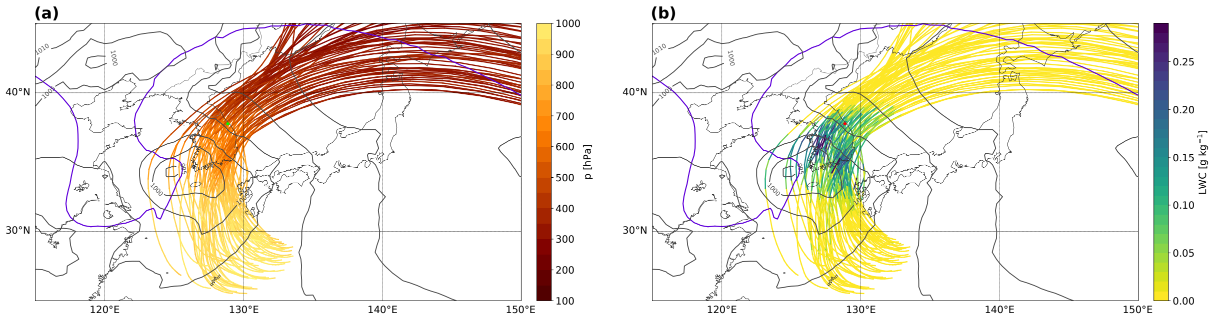

Figure 3. WCB trajectories with an ascent rate of at least 600 hPa in 48 h that are located near the measurement site at 06:00 UTC 28 February ~~2018 (red asterisk).~~ 2018. Colours indicate (a) the pressure level and (b) the LWC along the WCB air parcels. Also shown is sea level pressure (grey contours, every 5 hPa) and the dynamical tropopause at 315 K (purple). Only the WCB trajectories close to the site (green asterisk on (a) and red on (b)) are shown.

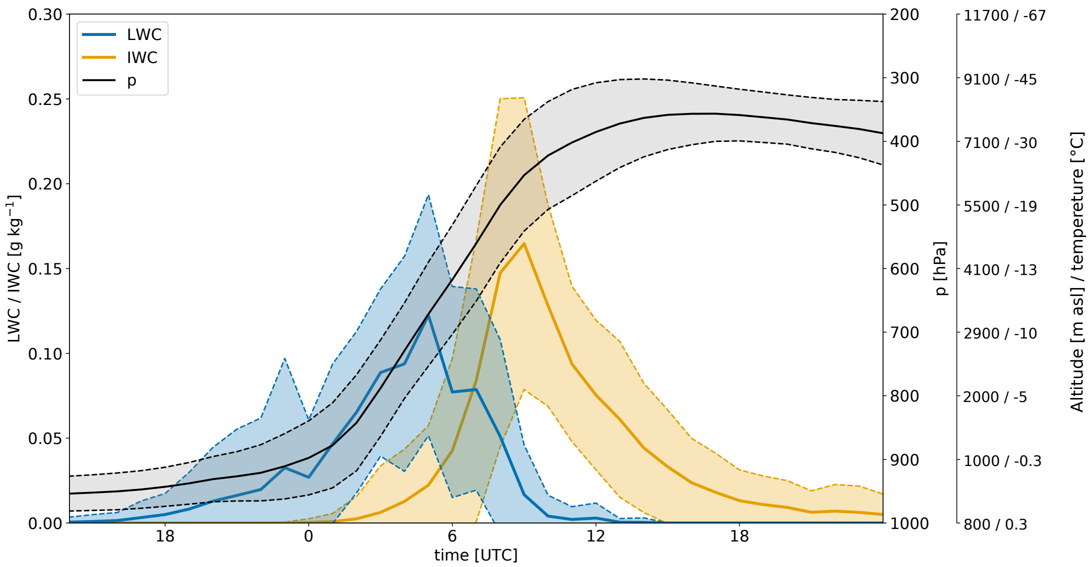

Figure 4. Temporal evolution of LWC (blue line, in $\mathrm{g\,kg^{-1}}$) and ice water contents (IWC, yellow line, in $\mathrm{g\,kg^{-1}}$) from IFS analyses along the WCB trajectories (black line and grey shading represent the pressure level of the selected trajectories, in hPa) shown in Fig. 3. Shown are the mean (solid lines) and the standard deviation (dashed lines and shading). The altitudes and temperatures of the pressure levels (second right y-axis) are taken from the radiosounding at 06:00 UTC.

~~Radiosoundings at DGW station showing (a) temperature (dashed lines) and equivalent potential temperature (solid lines), (b) relative humidity with respect to liquid (RHl, solid lines) and ice (RHi, dashed lines), (c) wind speed and (d) wind direction at 00:00 UTC (black), 06:00 UTC (cerise) and 09:00 UTC (blue) 28 February 2018. The diamonds symbols for the radiosoundings at 06:00 and 09:00 UTC show the altitude of the lower limit of the WCB (black contour in Fig. 5a,b,c).~~

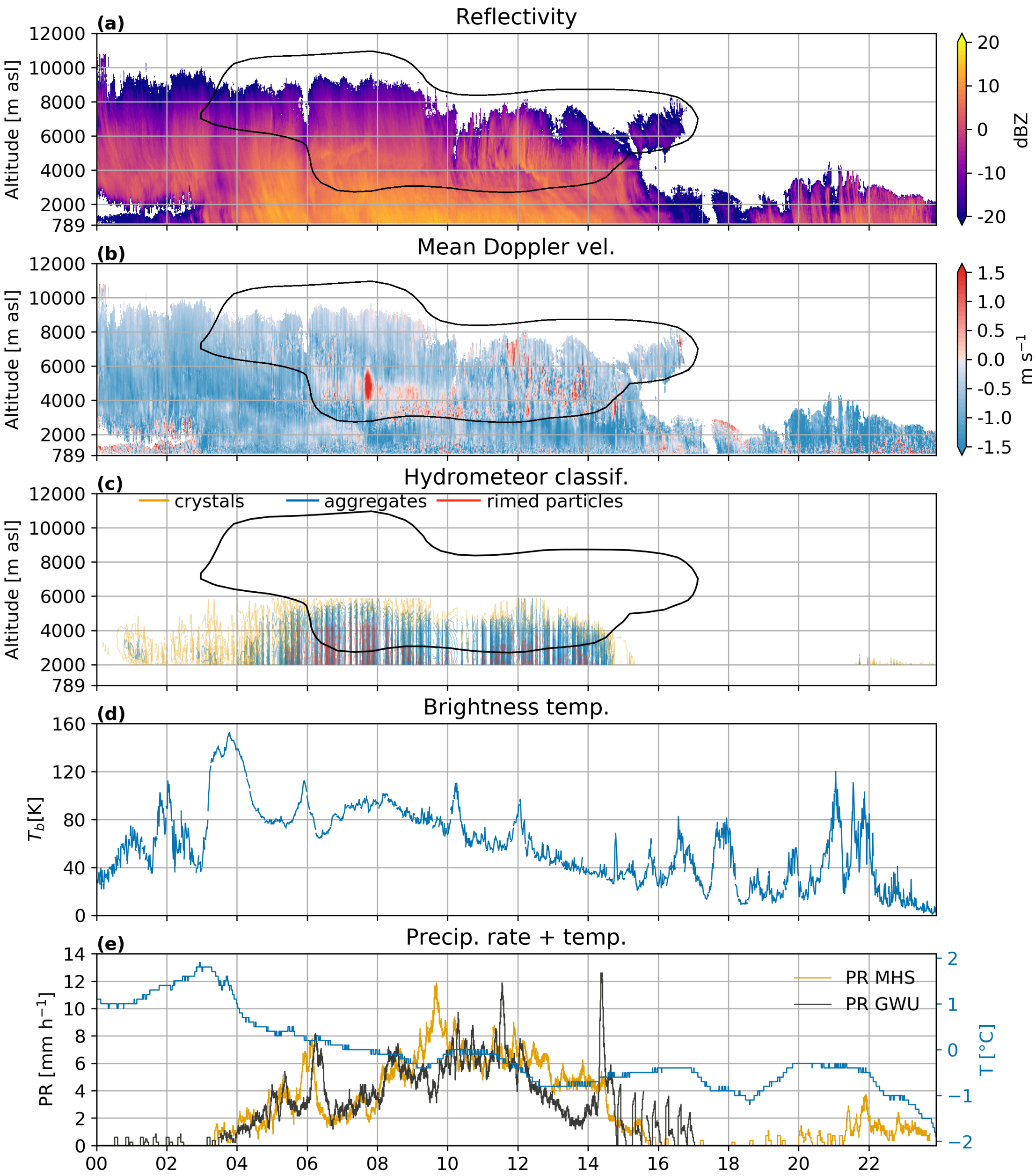

Figure 5. Time series on 28 February 2018 of (a) reflectivity and (b) mean Doppler velocity from WProf (defined positive upwards), (c) hydrometeor classification (Besic et al., 2018) based on MXPol RHIs towards MHS. Only data with an elevation angle between 5°and 45°are considered. The isolines represent the proportion of each hydrometeor class normalised by the average number of pixels per time step. The contour interval is 2 %. The ~~blue~~ yellow contours represent crystals, the ~~yellow~~ blue ones aggregates and the ~~cerise~~ red ones rimed particles. The results are shown only above 2000 m since the lower altitudes are contaminated by ground echoes. The black contour on panels (a), (b) and (c) shows the boundary of the WCB based on the projection of the trajectories in an Eulerian reference frame (see Sect. 2.4). (d) Brightness temperature (T_b) from the radiometer, (e) precipitation rate (PR, Pluvio^2 weighing rain gauge) in MHS (~~cerise~~yellow) and GWU (~~yellow~~black) and temperature in MHS (blue).

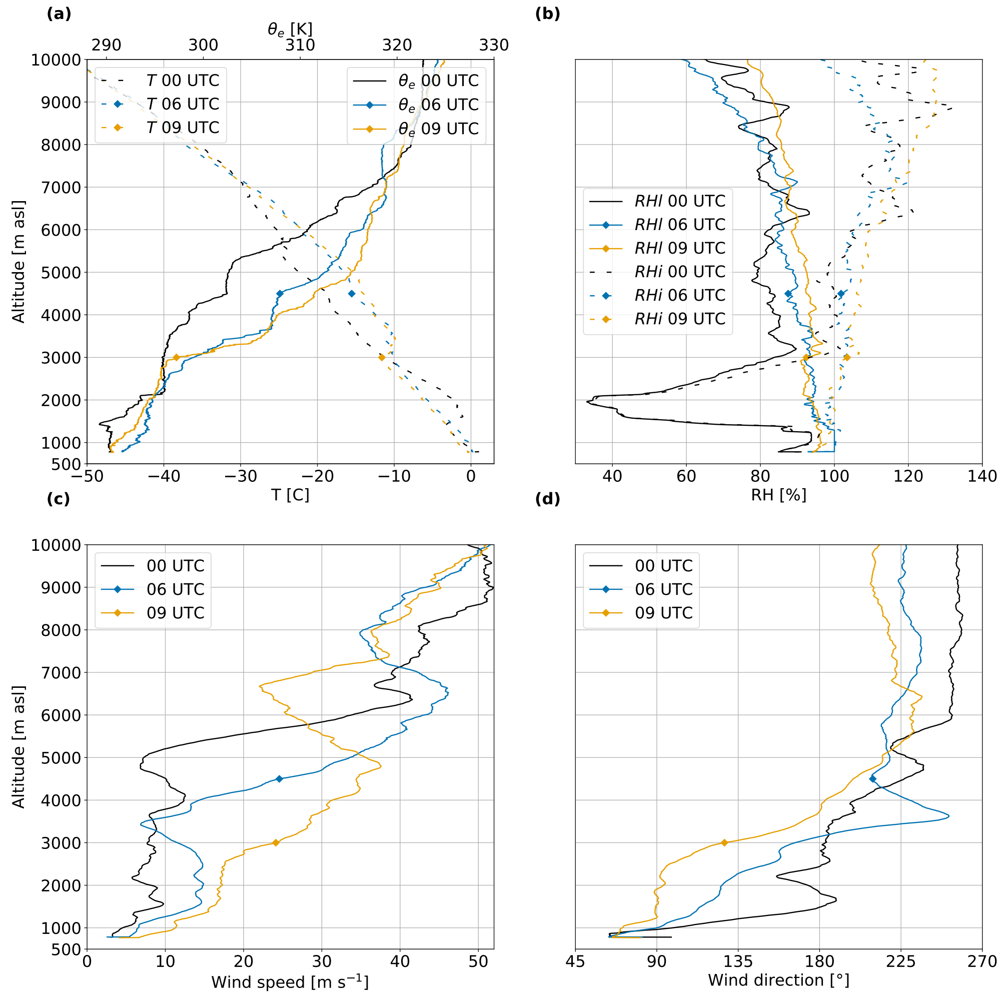

Figure 6. Radiosoundings at DGW station showing (a) temperature (dashed lines) and equivalent potential temperature (solid lines), (b) relative humidity with respect to liquid (RHl, solid lines) and ice (RHi, dashed lines), (c) wind speed and (d) wind direction at 00:00 UTC (black), 06:00 UTC (cerise) and 09:00 UTC (blue) 28 February 2018. The diamonds symbols for the radiosoundings at 06:00 and 09:00 UTC show the altitude of the lower limit of the WCB (black contour in Fig. 5a,b,c).

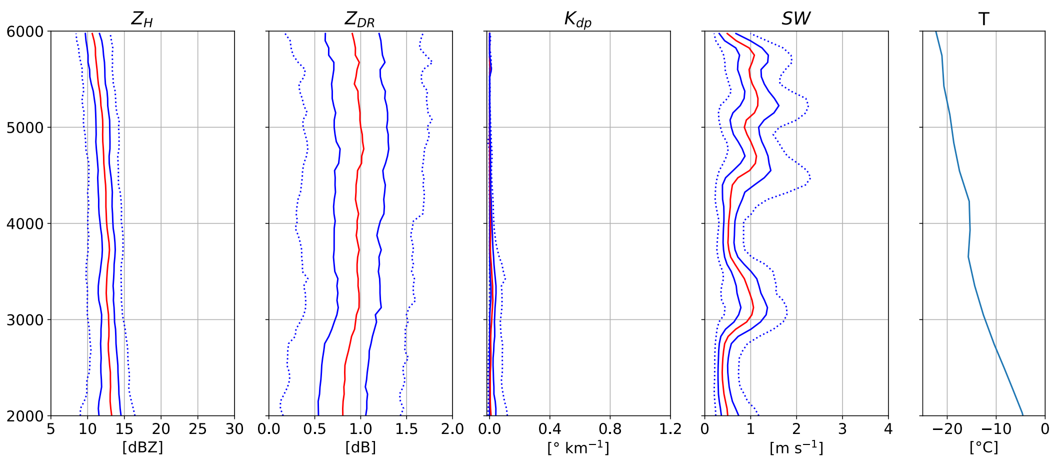

Figure 7. Vertical profiles of quantiles of Z_H, Z_{DR}, K_{dp} and SW from MXPol from 03:00 to 04:00 UTC 28 February 2018. The red line shows the median, while the blue solid lines show the 25th and 75th percentiles and the blue dotted lines the 5th and 95th percentiles. The statistics are based on 11 RHIs towards the MHS site. The data within an horizontal distance of 7 to 20 km from MXPol is selected. The black dashed line shows the lower limit of the WCB (black contour in Fig. 5a,b,c).

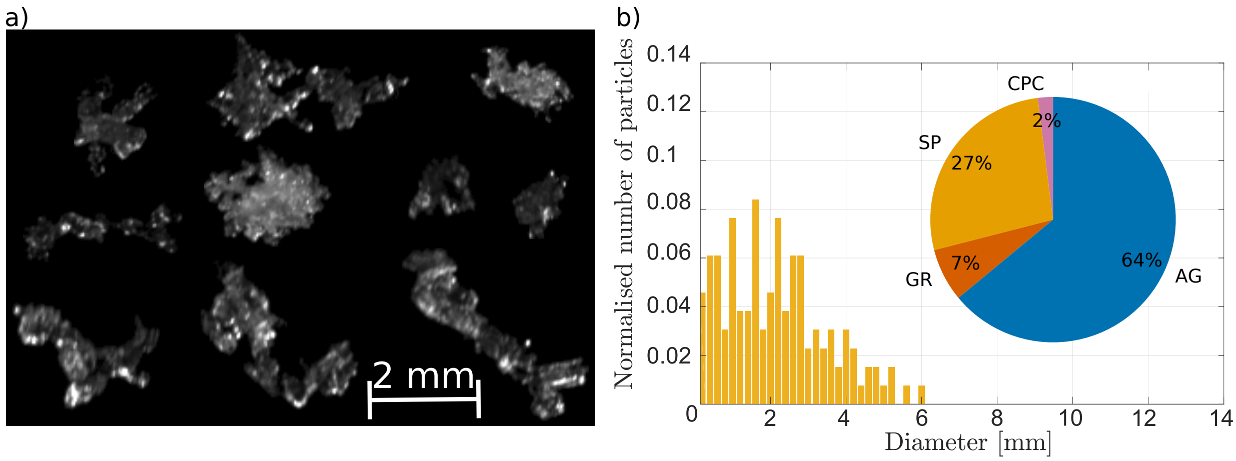

Figure 8. (a) Selection of in-focus MASC images. (b) Normalised size distribution and classification of ~~131~~ 55 particles observed from 03:00 to 04:00 UTC. SP are small particles, CC columnar crystals, PC planar crystals, AG aggregates, GR graupel and CPC combination of planar and columnar crystals. The size distribution is normalised by the number of particles. ~~(b) Selection~~ The pictures of ~~in-focus MASC images. We chose~~ panel (a~~set that was~~) were selected to be representative of the classification~~shown in panel~~. The average temperature was 1.5 °C (~~b~~Fig. 5e).

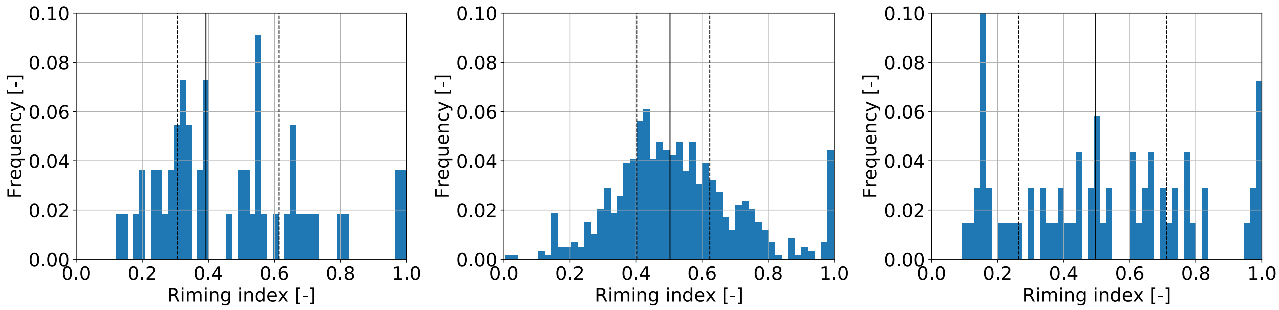

Figure 9. Distribution of the riming index for all particles between 03:00–04:00 UTC (a), 06:00–08:00 UTC (b) and 09:00–11:00 UTC (c). The dashed lines show the lower and upper quartiles, the solid line shows the median of the distribution.

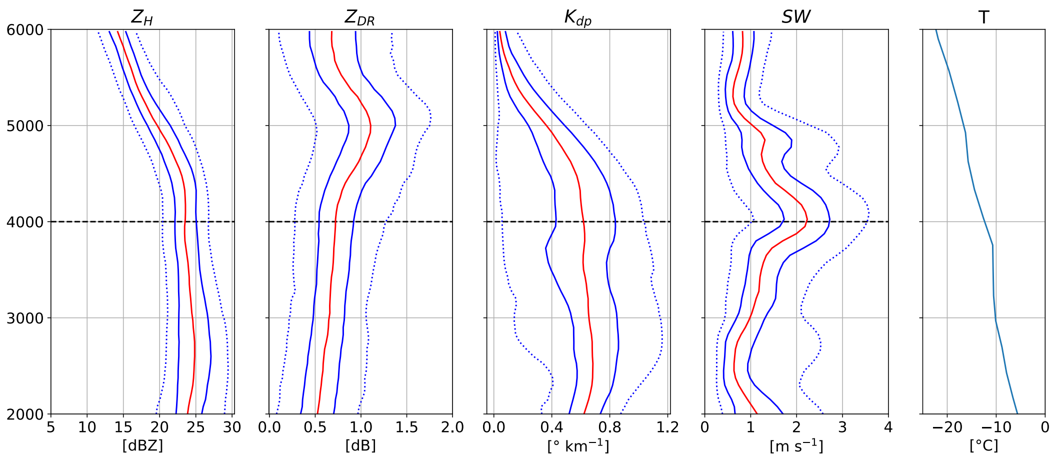

Figure 10. Same as Fig. 7 for 06:00 to 08:00 UTC 28 February 2018. The statistics are based on 21 RHIs towards the MHS site. The black dashed line shows the lower limit of the WCB (black contour in Fig. 5a,b,c).

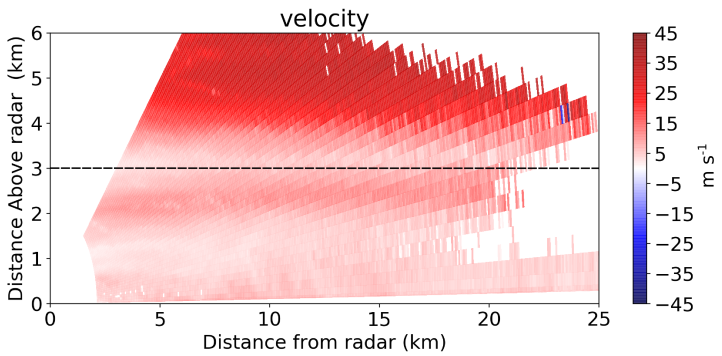

Figure 11. RHI of Doppler velocity at 11°azimuth at 06:25 UTC from MXPol radar. The black dashed line shows the lower limit of the WCB (black contour in Fig. 5a,b,c). The Python ARM Radar Toolkit (Py-ART) Helmus and Collis, 2016 was used to plot the radar data.

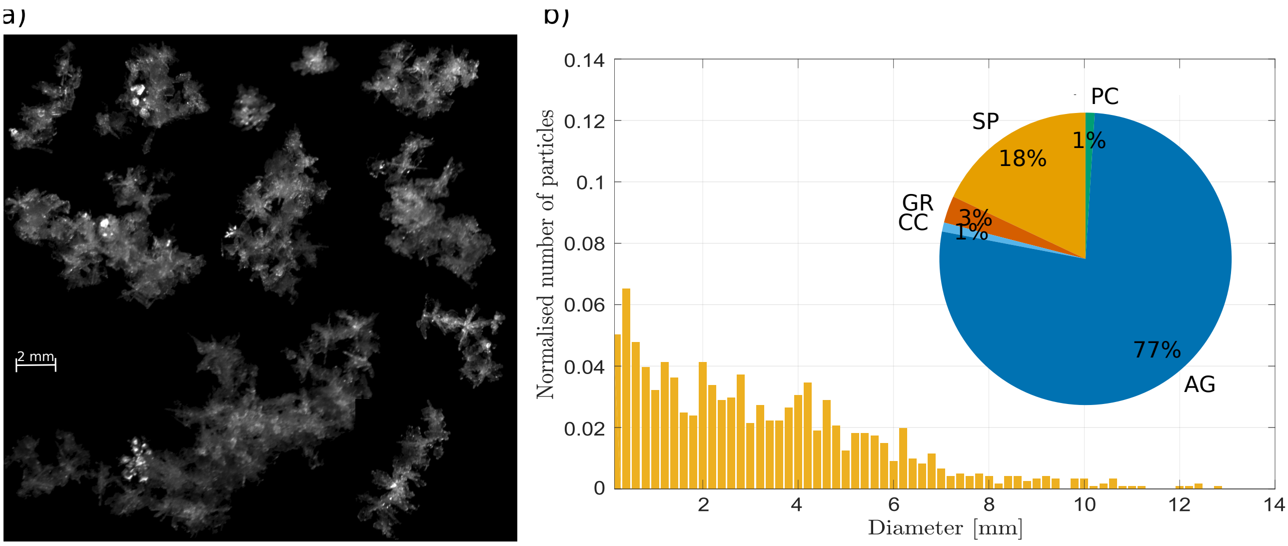

Figure 12. Same as Fig. 8 for the period 06:00 to 08:00 UTC. The number of particles is 589. The average temperature was 0.1 °C (Fig. 5e).

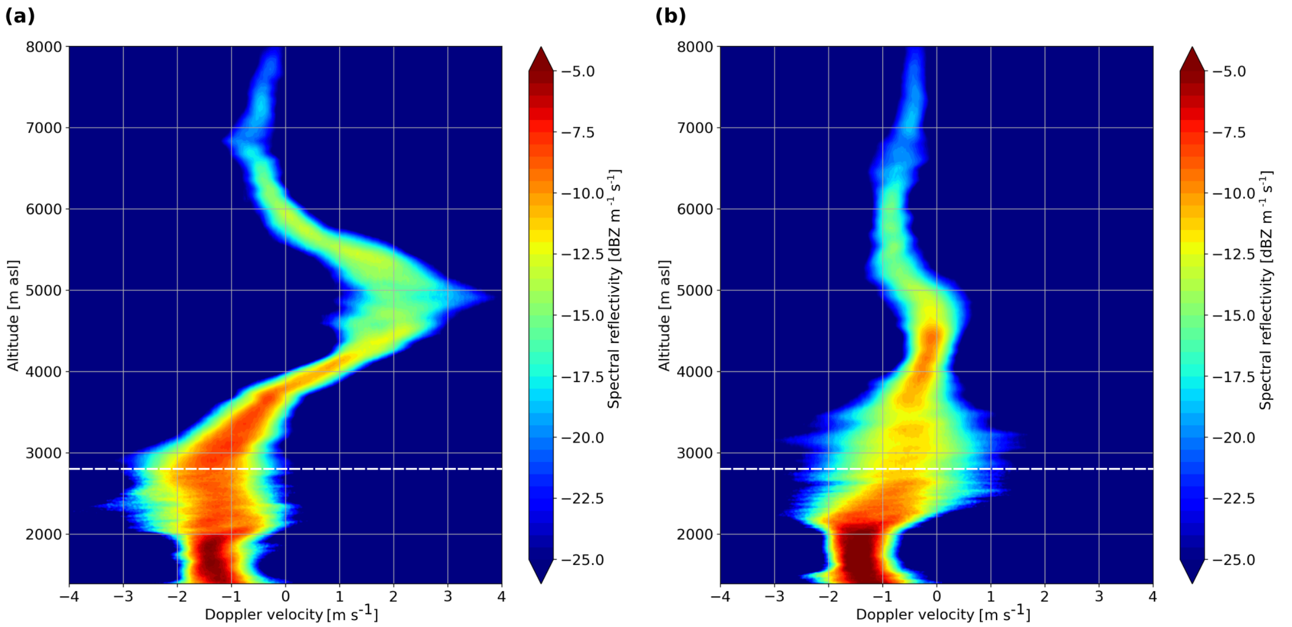

Figure 13. Range spectrogram from WProf averaged from 07:42 UTC to 07:47 UTC (a) and from 07:57 UTC to 08:02 UTC (b). Positive velocity values represent upward motions. The white dashed line shows the lower limit of the WCB (black contour in Fig. 5a,b,c).

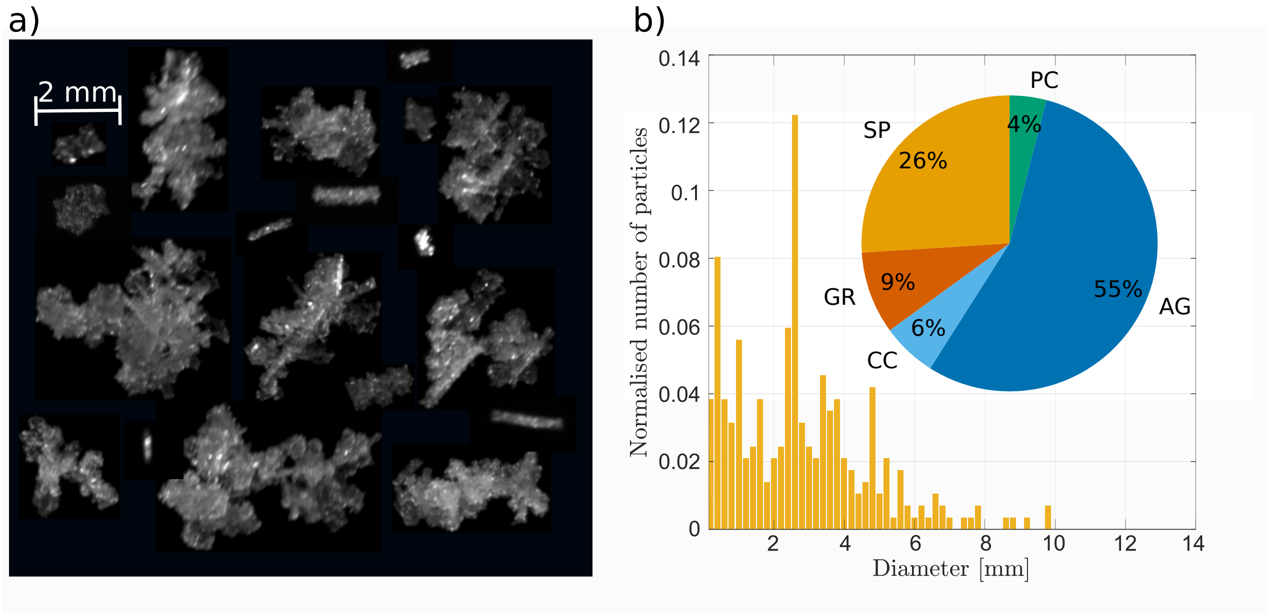

Figure 14. Same as Fig. 8 for the period 10:00 to 11:00 UTC. The number of particles is 69. The average temperature was 0.0 °C (Fig. 5e).

~~Time spectrogram from WProf at 5000 . The gaps are due to updates of the file acquisition system which was set to 5 during the campaign. Positive velocity values represent upward motions.~~

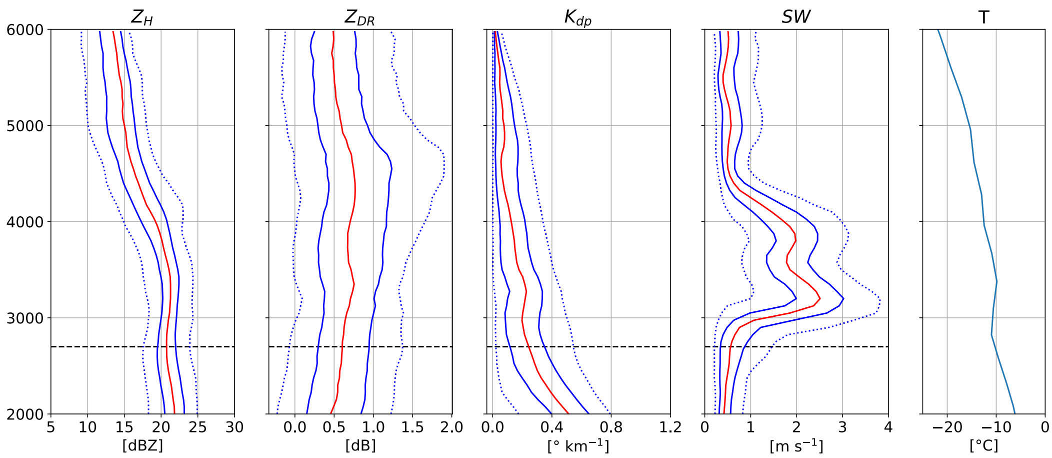

Figure 15. Same as Fig. ~~14~~ 7 for 09:00 to 11:00 UTC 28 February 2018. The statistics are based on 20 RHIs towards the MHS site. The black dashed line shows the lower limit of the WCB (black contour in Fig. 5a,b,c).

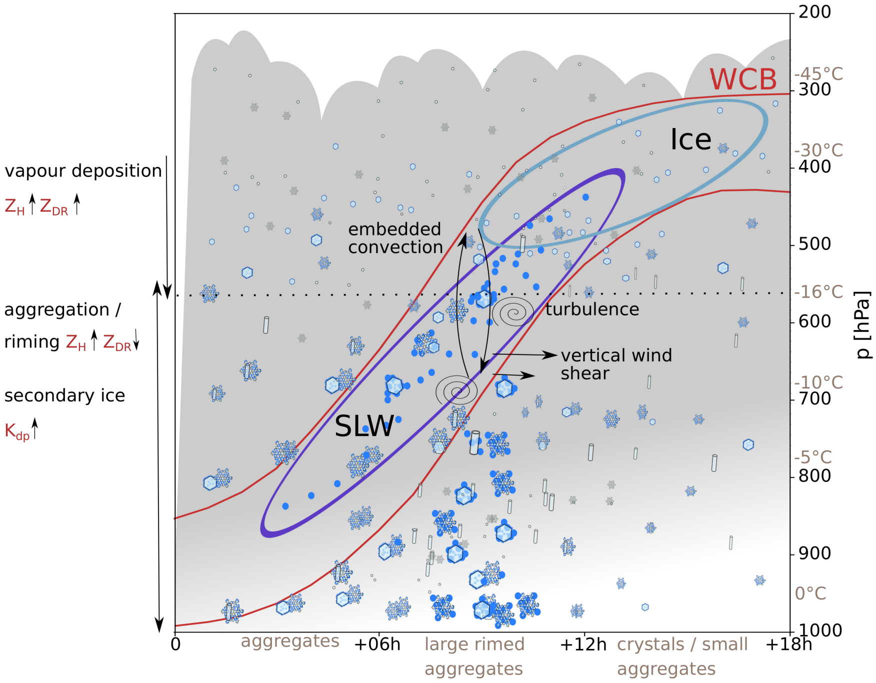

Figure 16. Conceptual model in a Lagrangian reference frame (i.e. along the WCB) summarising the key findings. The temperature indications come from the radiosounding at 06:00 UTC (Fig. 6a). The time is indicated as hours from the start of the ascent. The ascent is representative of a strong wintertime WCB.

Table 1. Description of WProf chirps

	Range	Range resolution	Doppler interval	Doppler resolution
chirp2	[2016, 9984] m	32.5 m	[-5.1, 5.1] $\mathrm{m\,s^{-1}}$	0.020 $\mathrm{m\,s^{-1}}$
chirp1	[603, 1990] m	11.2 m	[-5.1, 5.1] $\mathrm{m\,s^{-1}}$	0.020 $\mathrm{m\,s^{-1}}$
chirp0	[100, 598] m	5.6 m	[-7.16, 7.13] $\mathrm{m\,s^{-1}}$	0.028 $\mathrm{m\,s^{-1}}$

Table 2. Specifications of MXPol and WProf

Specifications	MXPol	WProf
Frequency	9.4 GHz	94 GHz
3 dB beamwidth	1.27°	0.53°
Range resolution	75 m	5.6, 11.2 and 32.5 m
transmission type	pulsed	FMCW

Table A1. Values of the different variables used in the computation of U_z^*. Data from IFS analysis and radiosoundings at 09:00 UTC are used. The pressure p used is 610 hPa temperature T is -13 °C

Variable	Value	Source
q_i	$1 \cdot 10^{-4}$ kg kg^{-1}	from IFS analysis Fig 4
q_s	$6.5 \cdot 10^{-4}$ kg kg^{-1}	from IFS analysis
ρ_i	920 kg m^{-3}	density of ice
ρ	0.82 kg m^{-3}	At p = 610 hPa, T = -13 °C and RHl = 95%
e_{si}	198 Pa	At p = 610 hPa, T = -13 °C and RHl = 95%
e_{sl}	224 Pa	At p = 610 hPa, T = -13 °C and RHl = 95%
N_i	2895 m^{-3}	Eq. A1
Λ	804	Eq. A3
N_s	2490 m^{-3}	Eq. A2
r_{tot}	309 µm	Eq. A7